

**1 Local wind regime induced by giant linear dunes:  
2 comparison of ERA5-Land reanalysis with surface  
3 measurements**

**4 Cyril Gadal · Pauline Delorme ·  
5 Clément Narteau · Giles F.S. Wiggs ·  
6 Matthew Baddock · Joanna M. Nield ·  
7 Philippe Claudin**

**8**  
**9 Received: DD Month YEAR / Accepted: DD Month YEAR**

**10 Abstract**

11 Emergence and growth of sand dunes results from the dynamic interaction  
12 between topography, wind flow and sediment transport. While feedbacks be-  
13 tween these variables are well studied at the scale of a single and relatively  
14 small dune, the average effect of a periodic large-scale dune pattern on atmo-  
15 spheric flows remains poorly constrained, due to a lack of data in major sand  
16 seas. Here, we compare local measurements of surface winds to the predictions  
17 of the ERA5-Land climate reanalysis at four locations in Namibia, within and  
18 outside the giant linear dune field of the Namib sand sea. In the desert plains  
19 to the north of the sand sea, observations and predictions agree well. This  
20 is also the case in the interdune areas of the sand sea during the day. Dur-  
21 ing the night, however, an additional wind component aligned with the giant  
22 dune orientation is measured, in contrast to the easterly wind predicted by

---

C. Gadal  
Institut de Mécanique des Fluides de Toulouse, Université de Toulouse Paul Sabatier, CNRS,  
Toulouse INP-ENSEEIHT, Toulouse, France. E-mail: cyril.gadal@imft.fr

P. Delorme  
Energy and Environment Institute, University of Hull, Hull, UK.

C. Narteau  
Institut de Physique du Globe de Paris, Université de Paris, CNRS, Paris, France.

G. Wiggs  
School of Geography and the Environment, University of Oxford, Oxford, UK.

M. Baddock  
Geography and Environment, Loughborough University, Loughborough, UK.

J.M. Nield  
School of Geography and Environmental Science, University of Southampton, Southampton,  
UK.

P. Claudin  
Physique et Mécanique des Milieux Hétérogènes, CNRS, ESPCI Paris, PSL Research Uni-  
versity, Université de Paris, Sorbonne Université, Paris, France.

the ERA5-Land reanalysis. For the given dune orientation and measured wind regime, we link the observed wind deviation (up to 50°) to the daily cycle of the turbulent atmospheric boundary layer. During the night, a shallow boundary layer induces a flow confinement above the giant dunes, resulting in large flow deviations, especially for the lower easterly winds. During the day, the feedback of the giant dunes on the atmospheric flow is much weaker due to the thicker boundary layer and higher wind speeds. Finally, we propose that the confinement mechanism and the associated wind deflections induced by giant dunes could explain the development of smaller-scale secondary dunes, elongating obliquely in the interdune areas of the primary dune patterns.

**Keywords** Atmospheric boundary layer · Sand dunes · Flow over hills

---

**34 1 Introduction**

35 The description of turbulent flows over complex topography is relevant for  
36 a large variety of different environmental systems (Sherman 1978; Walmsley  
37 et al. 1982; Baines 1995; Wood 2000; Venditti et al. 2013; Finnigan et al.  
38 2020). For example, the flow over hills is of primary interest for wind power,  
39 meteorological and air pollution phenomena (Taylor et al. 1987). The proper-  
40 ties of these flows are also key to the understanding of geophysical phenom-  
41 ena, including the formation of wind-driven waves on the ocean surface (Sulli-  
42 van and McWilliams 2010), dissolution bedforms (Claudin et al. 2017; Guérin  
43 et al. 2020), or sedimentary ripples and dunes (Bagnold 1941; Charru et al.  
44 2013; Courrech du Pont 2015). Importantly, the troposphere presents a vertical  
45 structure, with a lower convective boundary layer, of typical kilometer-scale  
46 thickness, capped by a stably stratified region (Stull 1988). The largest topo-  
47 graphic obstacles, such as mountains, can therefore interact with this upper  
48 region and lead to internal wave generation or significant wind disturbances,  
49 such as lee-side downslope winds (Durran 1990).

50 Compared to hills and mountains, aeolian sand dunes offer idealized ele-  
51 vation profiles for the study of atmospheric turbulent flow over topographies,  
52 due to their smooth shape, free of canopies. Besides, dunes provide a rather  
53 wide range of scales, from decameters to kilometers, and very often come in  
54 a fairly regular pattern, which further simplifies the flow structure analysis.  
55 Past studies have highlighted two important topographic feedbacks on the  
56 wind flow close to the dune/hill surface. First is the effect on wind speed, with  
57 documented flow acceleration on upwind slopes (Weaver and Wiggs 2011) and  
58 deceleration on downwind slopes (Baddock et al. 2007), where the speed-up  
59 factor is essentially proportional to the obstacle aspect ratio (Jackson and Hunt  
60 1975). Under multidirectional wind regimes with frequent wind reversals, this  
61 speed-up effect induces large differences in the amplitude and orientation of  
62 the resultant sediment transport between flat sand beds and the dune crests  
63 (???). In addition, the maximum in wind velocity is typically shifted upwind  
64 of the obstacle crest (Jackson and Hunt 1975; Claudin et al. 2013). This be-  
65 haviour has been theoretically predicted by means of asymptotic analysis of  
66 a neutrally stratified boundary-layer flow over an obstacle of vanishing aspect  
67 ratio (Jackson and Hunt 1975; Mason and Sykes 1979; Sykes 1980; Hunt et al.  
68 1988; Belcher and Hunt 1998; Kroy et al. 2002). Experiments in flumes (Zilker  
69 et al. 1977; Zilker and Hanratty 1979; Frederick and Hanratty 1988; Poggi et al.  
70 2007; Bristow et al. 2022), in wind tunnels (Gong and Ibbetson 1989; Finnigan  
71 et al. 1990; Gong et al. 1996) and in field conditions at all scales (Taylor and  
72 Teunissen 1987; Claudin et al. 2013; Fernando et al. 2019; Lü et al. 2021),  
73 have also documented this effect. Interestingly, a similar behaviour exists for  
74 the pressure perturbation, but with a slight downwind shift for the pressure  
75 minimum (Claudin et al. 2021).

76 The second effect, much less studied, is the flow deflection that occurs when  
77 the incident wind direction is not perpendicular to the ridge crest. While pre-  
78 dicted to be small (less than 10°) in the linear regime valid for shallow topogra-

79 phy (Gadal et al. 2019), significant flow steering has been reported in the field  
80 on the downwind side of steep enough obstacles, such as well-developed sand  
81 dunes (Tsoar and Yaalon 1983; Sweet and Kocurek 1990; Walker and Nickling  
82 2002; Smith et al. 2017) and in particular coastal foredunes (e.g. Hunter et al.  
83 1983; Rasmussen 1989; Walker et al. 2006, 2009; Hesp et al. 2015; Walker  
84 et al. 2017; de Winter et al. 2020), mountain ranges (Kim et al. 2000; Lewis  
85 et al. 2008; Fernando et al. 2019), and valley topographies (Wiggs et al. 2002;  
86 Garvey et al. 2005).

87 Wind measurements over sand dunes has been mainly performed over small  
88 bedforms, typically a few meters high (corresponding to several tens of meters  
89 long) (e.g. Mulligan 1988; Hesp et al. 1989; Lancaster et al. 1996; Mckenna  
90 Neuman et al. 1997; Sauermann et al. 2003; Andreotti et al. 2002; Walker and  
91 Nickling 2002; Weaver and Wiggs 2011). For practical reasons, fewer studies  
92 performed similar measurements on giant dunes (Havholm and Kocurek 1988),  
93 with kilometer-scale wavelengths and heights of tens of meters. However, such  
94 large dunes provide a choice configuration for the study of turbulent flows over  
95 a complex topography. First, one expects larger wind disturbances for larger  
96 obstacles. Secondly, their large size can make them interact with the vertical  
97 structure of the atmosphere (Andreotti et al. 2009). Third, they usually form  
98 large patterns in sand seas and thus behave as rather clean periodic perturba-  
99 tions, in contrast with isolated dunes. Finally, because the morphodynamics of  
100 aeolian bedforms is strongly dependent on the local wind regime (Livingstone  
101 and Warren 2019), one can expect to see the consequences of windflow dis-  
102 turbance by large dunes on neighbouring small dunes (Brookfield 1977; Ewing  
103 et al. 2006). A similar effect is observed on the properties of impact ripple  
104 patterns due to the presence of dunes (Howard 1977; Hood et al. 2021).

105 Atmospheric flows have been much studied at the desert-scale with climate  
106 reanalyses based on global atmospheric models (Blumberg and Greeley 1996;  
107 Livingstone et al. 2010; Ashkenazy et al. 2012; Jolivet et al. 2021; Hu et al.  
108 2021; Gunn et al. 2021b), such as ERA-40, ERA-Interim or ERA5 (Uppala  
109 et al. 2005; Dee et al. 2011; Hersbach et al. 2020). However, the spatial resolu-  
110 tion of these reanalyses (tens of kilometers) implies average quantities that do  
111 not resolve the smaller scales of interest, which range from individual dunes  
112 to small mountains (Livingstone et al. 2010). Recently, the release of ERA5-  
113 Land has partly resolved this limitation by providing up to 70 years of hourly  
114 wind predictions at a 9 km spatial resolution (Muñoz-Sabater et al. 2021).  
115 However, its validity remains to be studied, especially in remote desert areas  
116 where assimilation of measured data is very low.

117 In this work, we compare local wind speeds and directions measured by  
118 meteorological stations at four different locations inside and north of the giant  
119 linear dune field of the Namib sand sea to the regional predictions of the ERA5-  
120 Land climate reanalysis. Where the meteorological stations are surrounded by  
121 a relatively flat environment, we show that local measurements and regional  
122 predictions agree well. The agreement is also good in the interdune areas of  
123 the sand sea, except for some weak winds blowing at night, which exhibit an  
124 additional component aligned with the giant dune orientation. These winds

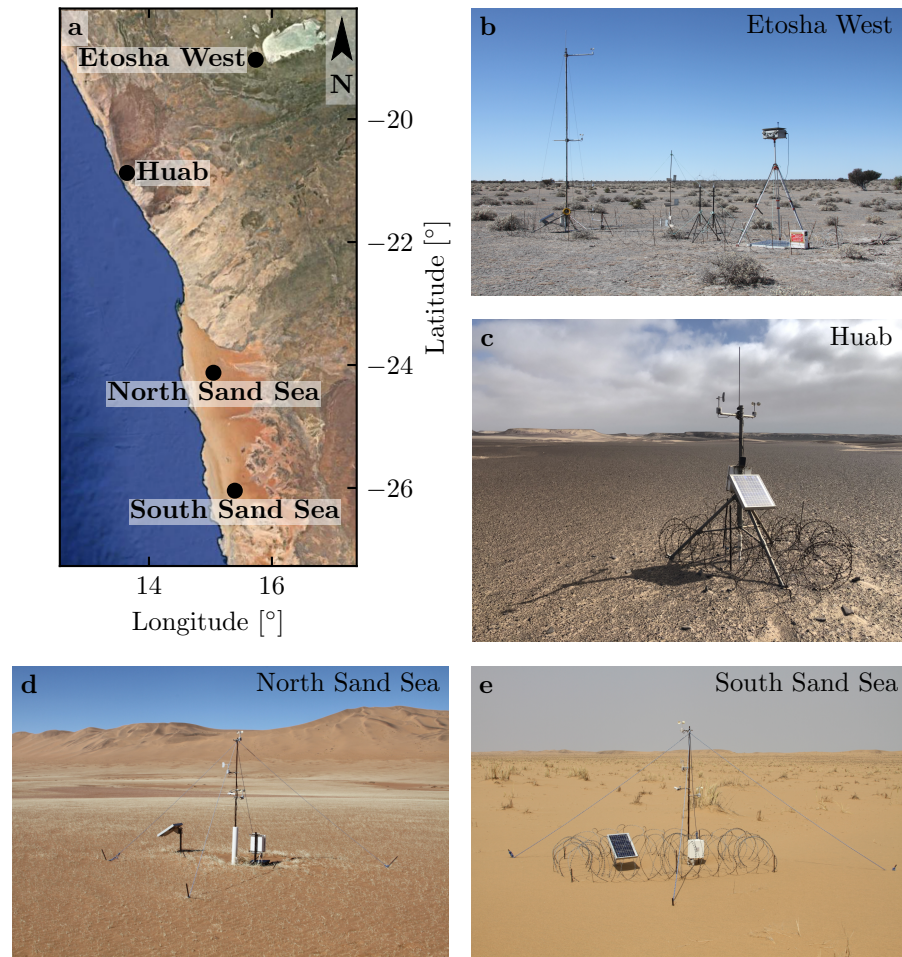


**Fig. 1** Studied field sites. **a:** Location of the different sites in Namibia. **b–e:** Photographs of the meteorological stations.

125 are not predicted by the ERA5-Land reanalysis (section 2). Further, we are  
 126 able to link the magnitude of these differences to the circadian cycle of the  
 127 atmospheric boundary layer (section 3). Finally, we draw implications for the  
 128 wind disturbances on smaller-scale dunes (section 4), suggesting a possible  
 129 origin for crossing dunes.

## 130 2 Wind regimes across the Namib Sand Sea

131 We measured the wind regime at four different locations in Namibia, represen-  
 132 tative of various arid environments across the Namib desert (Fig. 1, Fig. 2).  
 133 The Etosha West station was located at the Adamax waterhole to the west

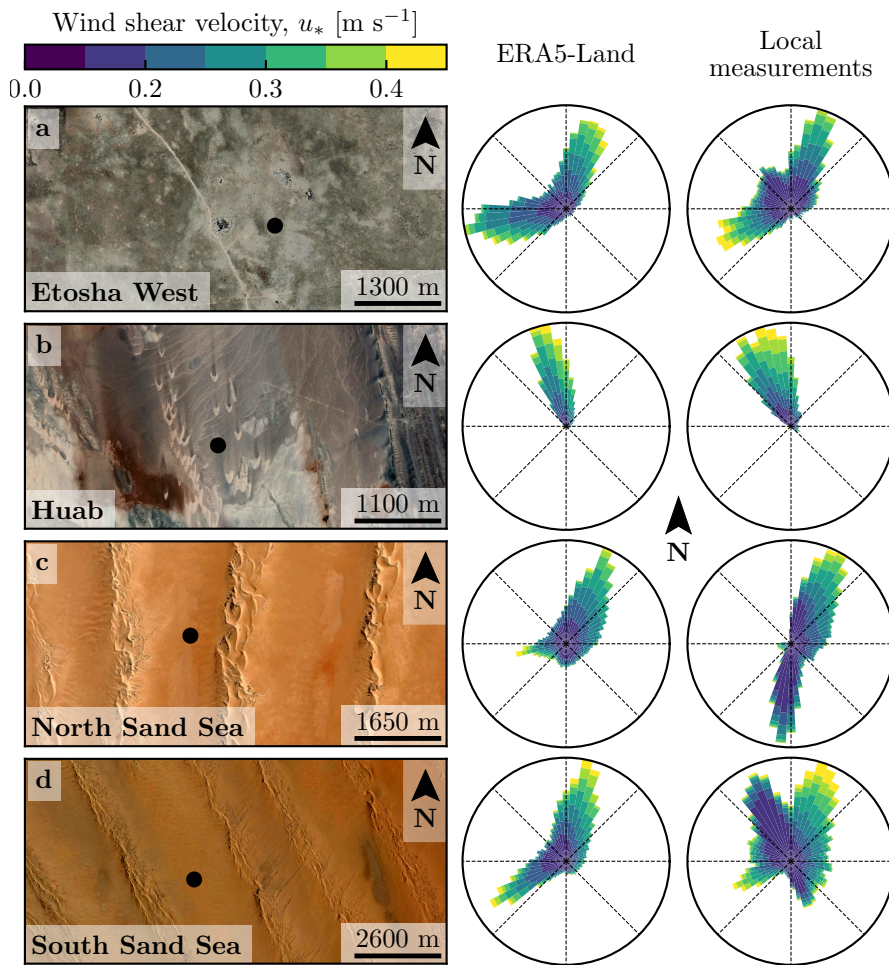


**Fig. 2** Wind data used in this study. Satellite images of the different environments (Google-Earth, Maxar Technologies, CNES/Airbus) are shown on the left. The black dots show the location of the wind measurements stations. On the right of the photos, the corresponding wind roses representing the data from the ERA5-Land climate reanalysis and the local wind stations are displayed. Note: the graphical convention for the wind roses is that the bars show the direction towards which the wind blows (see color bar for velocity scale).

of Etosha Pan in northern Namibia, in a sparsely vegetated area. The Huab station was near the coast on a hyper-arid flat gravel plain lying north the ephemeral Huab river. Here, barchan dunes up to a few meters in height develop from the sediment blowing out of the river valley (Nield et al. 2017; Hesp and Hastings 1998). These two stations were both located in relatively flat environments. In contrast, the North Sand Sea and South Sand Sea stations were located in the interdunes between linear dunes with kilometer-scale wavelengths, hectometer-scale heights and superimposed patterns. In this sec-

<sup>142</sup> tion, we describe and compare winds from local measurements and climate  
<sup>143</sup> reanalysis predictions.

<sup>144</sup> 2.1 Wind and elevation data

<sup>145</sup> At each meteorological station (Fig. 1), wind speed and direction were sampled  
<sup>146</sup> every 10 minutes using cup anemometers (Vector Instruments A100-LK) and  
<sup>147</sup> wind vanes (Vector Instruments W200-P) at a single height, which was between  
<sup>148</sup> 2 m and 3 m depending on the station. The available period of measurements at  
<sup>149</sup> each station ranged from 1 to 5 discontinuous years distributed between 2012  
<sup>150</sup> and 2020 (Online Resource Fig. S1). We checked that at least one complete  
<sup>151</sup> seasonal cycle was available for each station. Regional winds were extracted  
<sup>152</sup> at the same locations and periods from the ERA5-Land dataset, which is a  
<sup>153</sup> replay at a smaller spatial resolution of ERA5, the latest climate reanalysis  
<sup>154</sup> from the ECMWF (Hersbach et al. 2020; Muñoz-Sabater et al. 2021). This  
<sup>155</sup> dataset provided hourly predictions of the 10-m wind velocity and direction  
<sup>156</sup> at a spatial resolution of  $0.1^\circ \times 0.1^\circ$  ( $\simeq 9$  km in Namibia).

<sup>157</sup> To enable direct comparison, the local wind measurements were averaged  
<sup>158</sup> into 1-hr bins centered on the temporal scale of the ERA5-Land estimates  
<sup>159</sup> (Online Resource Fig. S2). As the wind velocities of both datasets were pro-  
<sup>160</sup> vided at different heights, we converted them into shear velocities  $u_*$  (Online  
<sup>161</sup> Resource section 1), characteristic of the turbulent wind profile. Wind roses  
<sup>162</sup> in Fig. 2 show the resulting wind data.

<sup>163</sup> Dune properties were computed using autocorrelation on the 30-m Digital  
<sup>164</sup> Elevation Models (DEMs) of the shuttle radar topography mission (Farr et al.  
<sup>165</sup> 2007). For the North and South Sand Sea stations, we obtain, respectively,  
<sup>166</sup> orientations of  $85^\circ$  and  $125^\circ$  with respect to the North, wavelengths of 2.6 km  
<sup>167</sup> and 2.3 km and amplitudes (or half-heights) of 45 m and 20 m (Online Resource  
<sup>168</sup> Fig. S4 for more details). This agrees with direct measurements made on site.

<sup>169</sup> 2.2 Comparison of local and regional winds

<sup>170</sup> The measured and predicted wind regimes are shown in Fig. 2. In the Namib,  
<sup>171</sup> the regional wind patterns are essentially controlled by the sea breeze, result-  
<sup>172</sup> ing in strong northward components (sometimes slightly deviated by the large  
<sup>173</sup> scale topography) present in all regional wind roses (Lancaster 1985). These  
<sup>174</sup> daytime winds are dominant during the period October-March (Fig. 3f and  
<sup>175</sup> Online Resource Fig. 4f). During April-September, an additional (and often  
<sup>176</sup> nocturnal) easterly component can also be recorded, induced by the combina-  
<sup>177</sup> tion of katabatic winds forming in the mountains, and infrequent ‘berg’ winds,  
<sup>178</sup> which are responsible for the high wind velocities observed (Lancaster et al.  
<sup>179</sup> 1984). The frequency of these easterly components decreases from inland to  
<sup>180</sup> the coast. As a result, bidirectional wind regimes within the Namib Sand Sea  
<sup>181</sup> and at the west Etosha site (Fig. 2a,c,d) and a unidirectional wind regime on  
<sup>182</sup> the coast at the outlet of the Huab River (Fig. 2b) are observed.

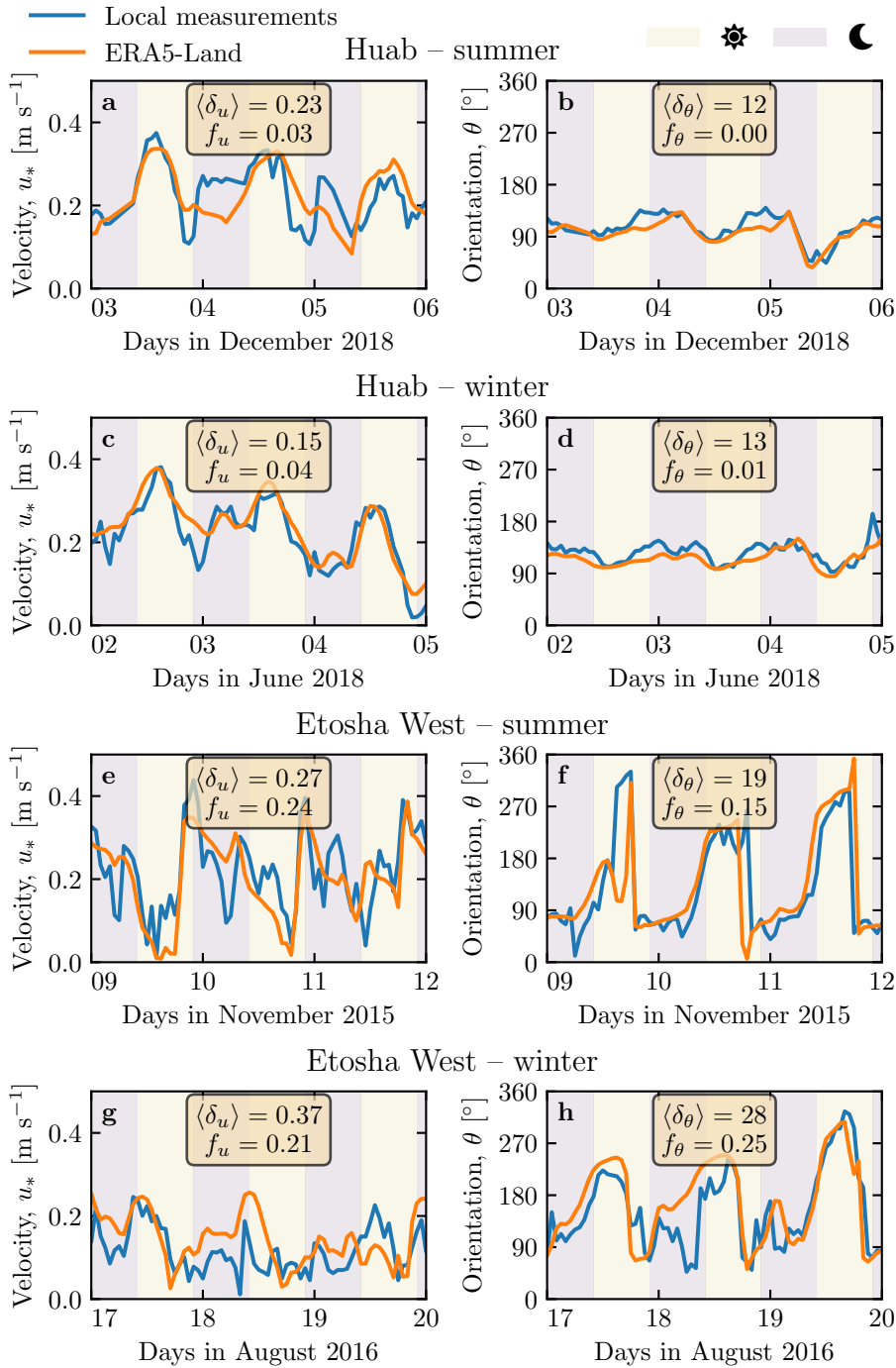


**Fig. 3** Temporal comparison between the wind data coming from the ERA5-Land climate reanalysis (orange lines) and from the local measurements (blue lines). Coloured swathes indicate day (between 10.00 UTC and 22.00 UTC) and night (before 10.00 UTC or after 22.00 UTC). Numbers in legends indicate the average flow deflection  $\delta_\theta$  and relative wind modulation  $\delta_u$  over the displayed period (see section 3.2 for their definitions), as well as the percentage  $f_\theta$  and  $f_u$  of occurrence of extreme events ( $\delta_\theta > 50^\circ$ ,  $|\delta_u| > 0.6$ ). **a–b**: Huab station in summer. **b–c**: Huab station in winter. **d–e**: Etosha West station in summer. **f–g**: Etosha West station in winter. Time series of the two other stations are shown in Fig. 5.

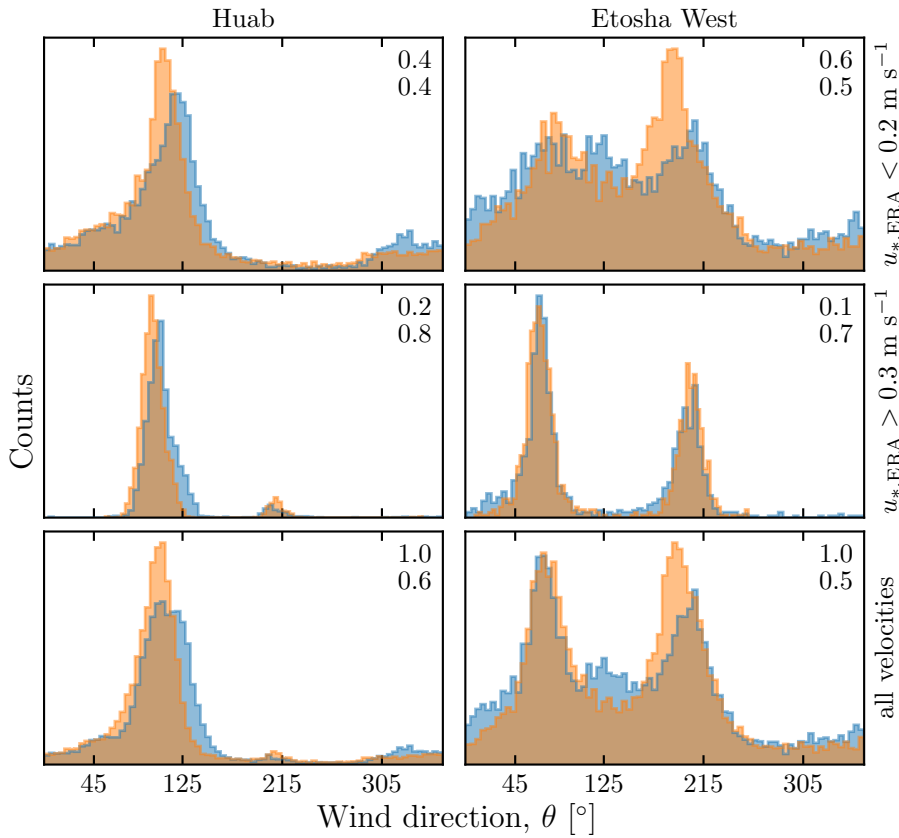


**Fig. 4** Distributions of wind direction at Huab and Etosha West stations for the ERA5-Land climate reanalysis (orange) and the local measurements (blue). In each subplot, both distributions are plotted from the same time steps, selected for different ranges of the wind wind velocity (rows) in the ERA5-Land dataset. The numbers at the upper right corners give the percentage of time steps selected in each sub-range (top), as well as the percentage of them corresponding to the day – defined between 10.00 UTC and 22.00 UTC (bottom).

In the case of the Etosha West and Huab stations, the time series of wind speed and direction from the regional predictions quantitatively match those corresponding to the local measurements (Figs. 3, 4 and Online Resource Fig. S5). For the North Sand Sea and South Sand Sea stations within the giant linear dune field, we observe that this agreement is also good, but limited to the October-March time period (Fig. 4a, b, e, f). However, the field-measured wind roses exhibit additional wind components aligned with the dune orientation, as evidenced on the satellite images (Fig. 2c,d).

More precisely, during the April-September period, the local and regional winds in the interdune match during daytime only, i.e. when the southerly/southwesterly sea breeze dominates (Figs. 5c,d,g,h and 6). In the late afternoon and during the night, when the easterly ‘berg’ and katabatic winds blow, measurements and predictions differ. In this case, the angular wind distribution of the lo-

cal measurements exhibits two additional modes corresponding to reversing winds aligned with the dune orientation (purple frame in Fig. 6, Online Resource Fig. S6). This deviation is also associated with a general attenuation of the wind strength (Online Resource Fig. S7). Remarkably, all these figures show that these wind reorientation and attenuation processes occur only at low velocities of the regional wind, typically for  $u_*^{\text{ERA5-Land}} \lesssim 0.2 \text{ m s}^{-1}$ . For shear velocities larger than  $u_*^{\text{ERA5-Land}} \simeq 0.3 \text{ m s}^{-1}$ , the wind reorientation is not apparent. Finally, for intermediate shear velocities, both situations of wind flow reoriented along the dune crest and not reoriented can be successively observed (Online Resource Fig. S6). Importantly, these values are not precise thresholds (and certainly not related to the threshold for sediment transport), but indicative of a crossover between regimes, whose physical interpretation is discussed in the next section.

### 209 3 Influence of wind speed and circadian cycle on the atmospheric 210 boundary layer

211 The wind deflection induced by dunes has previously been related to the in-  
212 cident angle between wind direction and crest orientation, with a maximum  
213 deflection evident for incident angles between  $30^\circ$  and  $70^\circ$  (Walker et al. 2009;  
214 Hesp et al. 2015). In the data analysed here, the most deflected wind at both  
215 the North and South Sand Sea stations is seen to be where the incident angle  
216 is perpendicular to the giant dunes (Figs. 2 and 6). It therefore appears that  
217 in our case, the incident wind angle is not the dominant control on maximum  
218 wind deflection. Further, and as shown in Fig. 6, winds of high and low veloc-  
219 ities show contrasting behaviour in characteristics of deflection. This suggests  
220 a change in hydrodynamical regime between the winds. In this section, we  
221 discuss the relevant parameters associated with the dynamical mechanisms  
222 that govern the interactions between the atmospheric boundary layer flow and  
223 giant dune topographies. This analysis allows us to provide a physics-based  
224 interpretation of our measured wind data.

#### 225 3.1 Flow over a modulated bed

226 Taking as a reference the turbulent flow over a flat bed, the general framework  
227 of our study is understanding and describing the flow response to a bed mod-  
228 ulation (e.g. a giant dune). Without loss of generality, we can consider in this  
229 context an idealised bed elevation in the form of parallel sinusoidal ridges, with  
230 wavelength  $\lambda$  (or wavenumber  $k = 2\pi/\lambda$ ) and amplitude  $\xi_0$ , and where the ref-  
231 erence flow direction makes a given incident angle with respect to the ridge  
232 crest (Andreotti et al. 2012). Part of this response, on which we focus here,  
233 is the flow deflection by the ridges. In a simplified way, it can be understood  
234 from the Bernoulli principle (Hesp et al. 2015): as the flow approaches the  
235 ridge crest, the compression of the streamlines results in larger flow velocities,

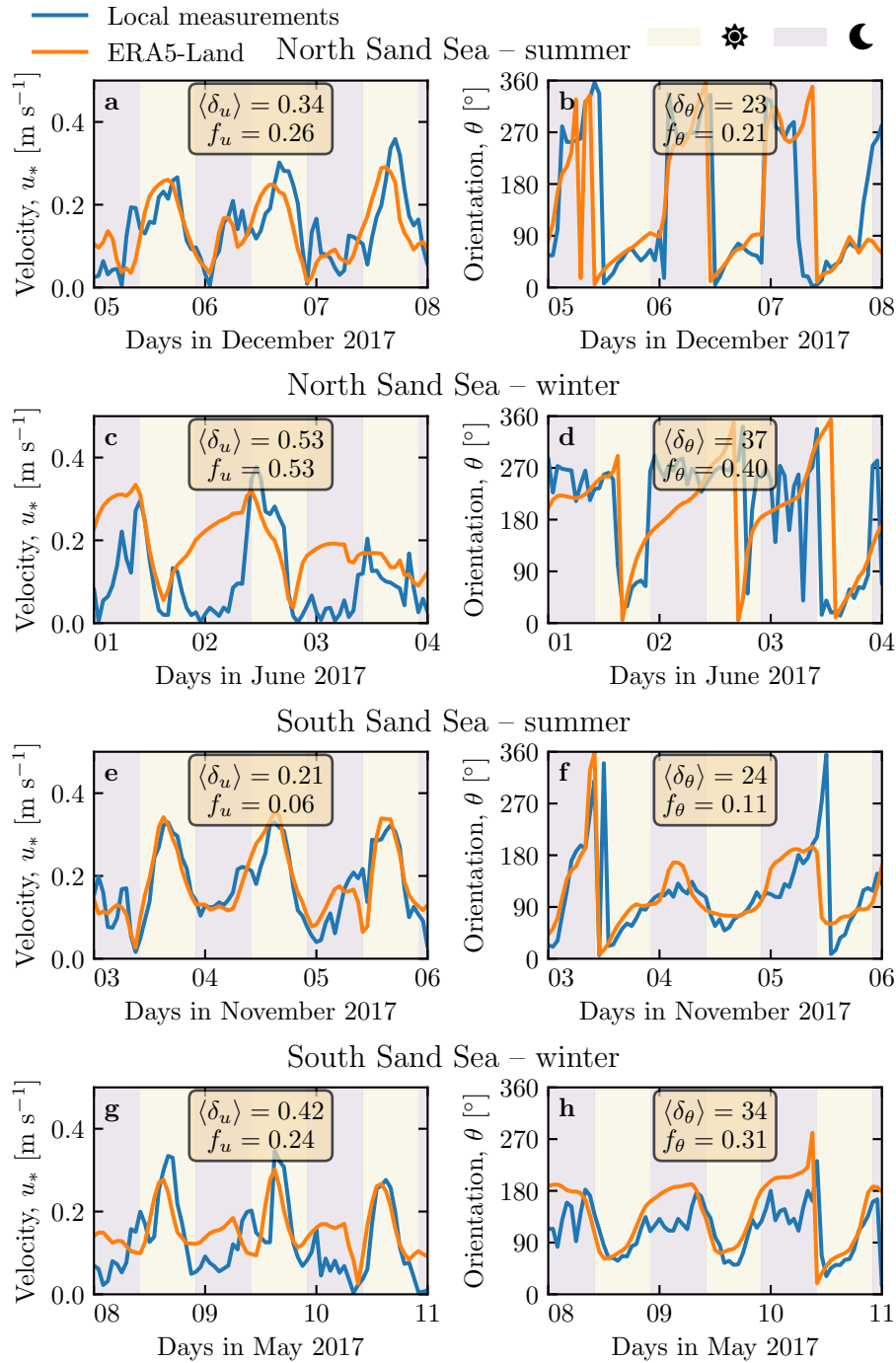


**Fig. 5** Same as Fig. 3 for North Sand Sea station in summer (a–b), North Sand Sea station in winter (b–c), South Sand Sea station in summer (d–e) and South Sand Sea station in winter (f–g).

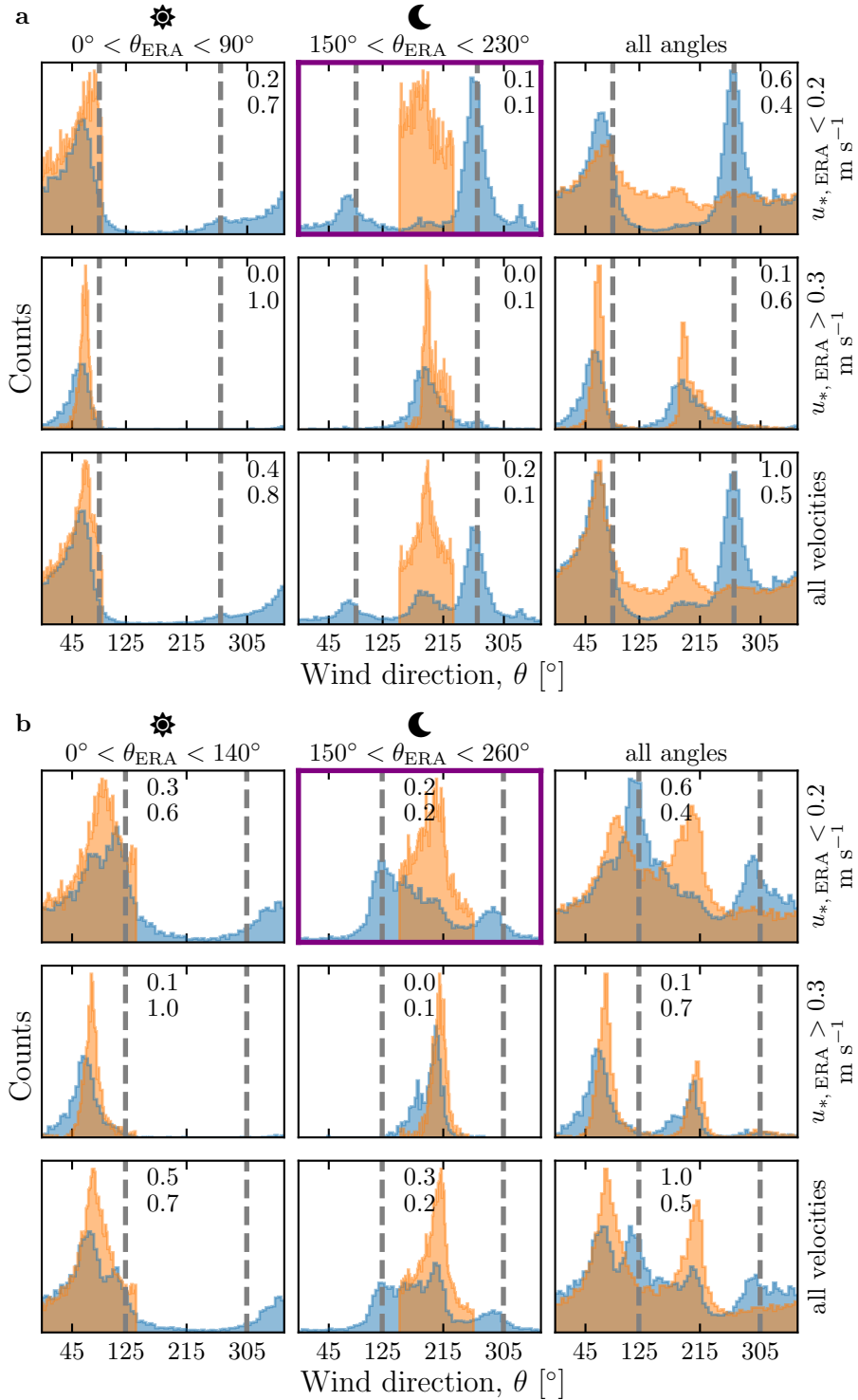


**Fig. 6** Same as Fig. 4 but for North Sand Sea (**a**) and South Sand Sea (**b**) stations. Here, subplots correspond to different ranges for the wind direction (columns) and wind velocity (rows) of the ERA5-Land dataset. The grey vertical dashed lines indicate the main dune orientation. In contrast with observations at the Huab and Etosha West stations (Fig. 4), histograms do not match well at low wind velocities, and the purple frame highlights the regime (low wind velocities, nocturnal easterly wind) in which the data from both datasets differ most.

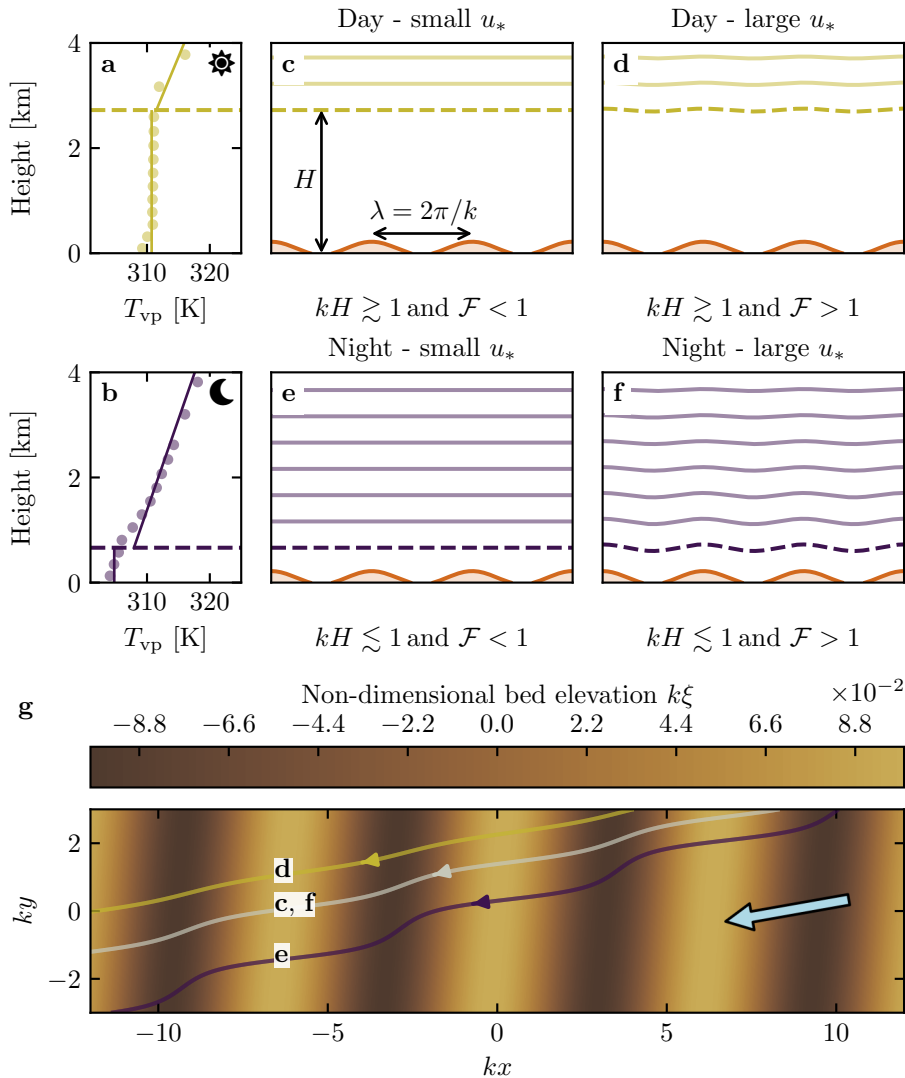


**Fig. 7** **a–b:** Vertical profiles of the virtual potential temperature  $T_{vp}$  at two different time steps (day - 03/11/2015 - 12.00 UTC, night - 01/13/2013 - 09.00 UTC) at the North Sand Sea station. Dots: data from the ERA5 reanalysis. Dashed lines: boundary layer height given by the ERA5 reanalysis (Online Resource section 2). Plain lines: vertical (boundary layer) and linear (free atmosphere) fits to estimate the stratification properties. **c–f:** Sketches representing the interaction between the giant dunes and the atmospheric flow for different meteorological conditions. **g:** Streamlines over a sinusoidal topography  $\xi(x, y)$  qualitatively representing the effect of low, medium and strong flow confinement, in relation to the above panels (see Appendix 1 for more details). The blue arrow indicates the undisturbed wind direction.

and thus lower pressures (Jackson and Hunt 1975). An incident flow oblique to the ridge is then deflected towards lower pressure zones, i.e towards the crest. Turbulent dissipation tends to increase this effect downstream, resulting in wind deflection along the crest in the lee side (Gadal et al. 2019).

Flow confinement below a capping surface, which enhances streamline compression, has a strong effect on the hydrodynamic response and typically increases flow deflection. This is the case for bedforms forming in open channel flows such as rivers (Kennedy 1963; Chang and Simons 1970; Mizumura 1995; Colombini 2004; Fourrière et al. 2010; Andreotti et al. 2012; Unsworth et al. 2018). This is also relevant for aeolian dunes as they evolve in the turbulent atmospheric boundary layer (ABL) capped by the stratified free atmosphere (FA) (Andreotti et al. 2009). Two main mechanisms, associated with dimensionless numbers must then be considered (Fig. 7). First, topographic obstacles typically disturb the flow over a characteristic height similar to their length. As flow confinement is characterised by a thickness  $H$ , the interaction between the dunes and the wind in the ABL is well captured by the parameter  $kH$ . The height  $H$  is directly related to the sensitive heat flux from the Earth surface. It is typically on the order of a kilometre, but significantly varies with the circadian and seasonal cycles. Emerging and small dunes, with wavelengths in the range 20 to 100 m, are not affected by the flow confinement, corresponding to  $kH \gg 1$ . For giant dunes with kilometer-scale wavelengths, however, their interaction with the FA can be significant (Andreotti et al. 2009). This translates into a parameter  $kH$  in the range 0.02–5, depending on the moment of the day and the season. A second important mechanism is associated with the existence of a thin intermediate so-called capping layer between the ABL and the FA. It is characterised by a density jump  $\Delta\rho$ , which controls the ‘rigidity’ of this interface, i.e. how much its deformation affects streamline compression. This is usually quantified using the Froude number (Vosper 2004; Stull 2006; Sheridan and Vosper 2006; Hunt et al. 2006; Jiang 2014):

$$\mathcal{F} = \frac{U}{\sqrt{\frac{\Delta\rho}{\rho_0}} g H}, \quad (1)$$

where  $U$  is the wind velocity at the top of the ABL and  $\rho_0$  its average density. The intensity of the stratification, i.e. the amplitude of the gradient  $|\partial_z \rho|$  in the FA, also impacts the ability to deform the capping layer under the presence of an underlying obstacle, and thus affects the influence of flow confinement. This can be quantified using the internal Froude number (Vosper 2004; Stull 2006; Sheridan and Vosper 2006; Hunt et al. 2006; Jiang 2014)  $\mathcal{F}_I = kU/N$ , where  $N = \sqrt{-g\partial_z \rho / \rho_0}$  is the Brunt-Väisälä frequency (Stull 1988). Both Froude numbers have in practice the same qualitative effect on flow confinement (a smaller Froude corresponding to a stiffer interface), and we shall restrict the main discussion to  $\mathcal{F}$  only.

With this theoretical framework in mind, and in the context of the measured wind data in the North and South Sand Sea stations, the smallest wind disturbances are expected to occur during the day, when the ABL depth is

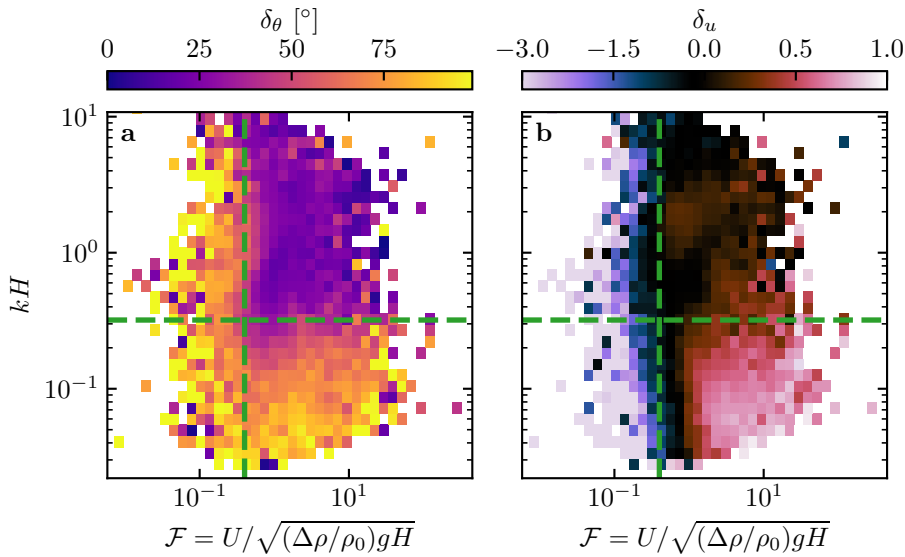


**Fig. 8** Regime diagrams of the wind deviation  $\delta_\theta$  (a) and relative attenuation/amplification  $\delta_u$  (b) in the space  $(\mathcal{F}, kH)$ , containing the data from both the North Sand Sea and South Sand Sea stations. The green dashed lines empirically delimit the different regimes. The point density in each bin of the diagrams is shown in Online Resource Fig. S10 – 95% of the data occur in the range  $-1 < \delta u < 1$ . Similar regime diagrams in the spaces  $(\mathcal{F}_I, kH)$  and  $(\mathcal{F}_I, \mathcal{F})$  are shown in Online Resource Fig. S11.

278 the largest and comparable to the dune wavelength ( $kH \gtrsim 1$ ), which corre-  
 279 sponds to a weak confinement situation (Fig. 7c,d). In contrast, large wind  
 280 disturbances are expected to occur during the night, when the confinement  
 281 is mainly induced by a shallow ABL (Fig. 7e). However, this strong confine-  
 282 ment can be somewhat reduced in the case of strong winds, corresponding to  
 283 large values of the Froude number and a less ‘rigid’ interface (Fig. 7f). This  
 284 is in qualitative agreement with the transition from deflected to non-deflected  
 285 winds related to low and high velocities observed in our data (Sec. 2.2).

### 286 3.2 Data distribution in the flow regimes

287 We can go one step further and analyse how our data quantitatively spread  
 288 over the different regimes discussed above. For that purpose, one needs to  
 289 compute  $kH$  and  $\mathcal{F}$  from the time series.  $H$ ,  $U$  and the other atmospheric  
 290 parameters can be deduced from the various vertical profiles (temperature,  
 291 humidity) available in the ERA5 climate reanalysis (Online Resource section  
 292 2). We quantify the flow deflection  $\delta_\theta$  as the minimal angle between the wind  
 293 orientations comparing the local measurements and the regional predictions.  
 294 We also compute the relative velocity modulation as

$$\delta_u = \frac{u_*^{\text{ERA5-Land}} - u_*^{\text{Local mes.}}}{u_*^{\text{ERA5-Land}}}. \quad (2)$$

These two quantities are represented as maps in the plane ( $\mathcal{F}$ ,  $kH$ ) (Fig. 8a,b), and one can clearly identify different regions in these graphs. Small wind disturbances (small  $\delta_\theta$  and  $\delta_u$ ) are located in the top-right part of the diagrams, corresponding to a regime with low-interaction as well as low-confinement ( $kH$  and  $\mathcal{F}$  large enough, Fig. 7d). Lower values of  $kH$  (stronger interaction) or of Froude number (stronger confinement) both lead to an increase in wind disturbances, both in terms of orientation and velocity. Below a crossover value  $kH \simeq 0.3$ , wind disturbance is less sensitive to the  $\mathcal{F}$ -value. This is probably due to enhanced non-linear effects linked to flow modulation by the obstacle when confinement is strong (e.g. wakes and flow recirculations). The Froude number also controls a transition from damped to amplified wind velocities in the interdune, with a crossover around  $\mathcal{F} \simeq 0.4$  (Fig. 8b). Such an amplification is rather unexpected. Checking the occurrence of the corresponding data, it appears that these amplifications are associated with the southerly sea breeze, and occur dominantly during the October-March period, when the other easterly wind is not present (Online Resource Fig. S12a–b). Furthermore, they occur less frequently during the afternoon, and more frequently at the end of the day (Online Resource Fig. S12c). This effect may be linked to a change in the flow behaviour in the lee side of the obstacles but further measurements are needed in order to assess the different possibilities (Baines 1995; Vosper 2004).

As the hydrodynamic roughness  $z_0$  determine the magnitude of wind shear velocities, Froude number  $\mathcal{F}$  and relative velocity modulation  $\delta_u$ , it is important to discuss the sensitivity of the results to the  $z_0$ -values chosen for both the ERA5-Land and the field data (see Online Resource section 4). Other quantities associated with wind direction are independent of this choice. Considering the possible range of realistic roughness values, the uncertainty on velocities estimated using the law of the wall is at most 30 %. A similar maximum uncertainty applies to the Froude number. This uncertainty also propagates to  $\delta_u$ , for which Figure S14 shows that the choice of roughness has little influence on its temporal variations, even if it can induce a global increase or decrease of its values. Hence, the choice of the  $z_0$ -values will not qualitatively affect the overall aspect of the regime diagram presented in Figure 8b. It may only change the value of  $\delta_u$  for which the transition between regimes is observed (dashed green lines in Figure 8b). Our conclusions are thus robust with respect to the somewhat arbitrary choice of the hydrodynamic roughness values.

#### 4 Discussion and conclusion

The feedback of the giant dunes on the wind flow has important implications for smaller scales bedforms. As illustrated in Fig. 9, small linear dunes ( $\sim 50$  m wide) are often present in the 1–2 km interdune between giant linear dunes in the Namib Sand Sea (Livingstone et al. 2010). These smaller dunes do not exhibit the same orientation as the large ones, and are sometimes named ‘crossing dunes’ (Chandler et al. 2022). Whilst differences between large and small

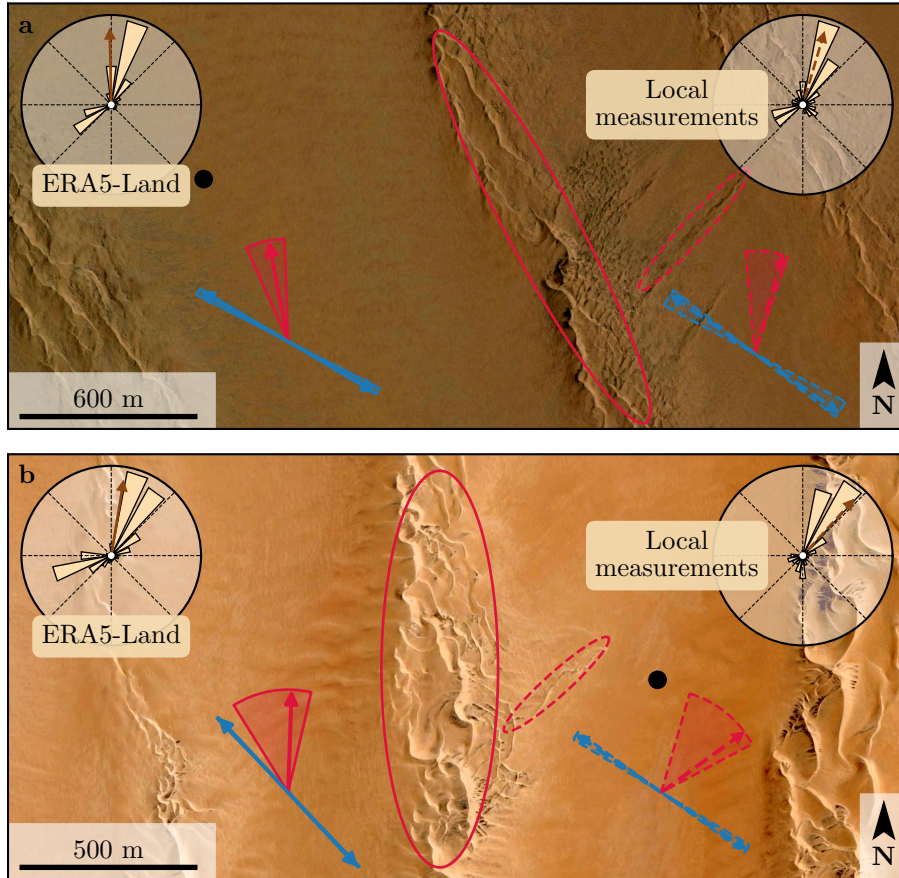


**Fig. 9** Implications for smaller scale patterns in (a) the South Sand Sea and (b) North Sand Sea. The ellipses indicate the different types of elongating dunes, at large (plain line) and small (dashed line) scales. Dune orientation are predicted using the model of Courrech du Pont et al. (2014) from the sand flux angular distributions, shown here (roses) along with the resultant transport direction (brown arrow) for typical values (grain size  $180 \mu\text{m}$ , flux-up ratio of 1.6). Code for corresponding arrows: use of ERA5-Land data (plain line), use of local measurements (dashed line), prediction for the bed instability growth mechanism (blue), prediction for the elongation growth mechanism (red). Wedges show the uncertainty on the orientation calculation when parameters are varied. The black dots indicate the location of the meteorological stations in the interdune. See Appendix 2 for additional details.

338 scale dune patterns are observed ubiquitously, they are usually attributed to  
 339 the presence of two different dune growth mechanisms, leading to two dif-  
 340 ferent dune patterns (orientations and/or morphologies) for the same wind  
 341 regime (Courrech du Pont et al. 2014; Runyon et al. 2017; Lü et al. 2017; Song  
 342 et al. 2019; Gadal et al. 2020; Hu et al. 2021). Here, however, our arguments  
 343 enable the development of differing orientations for the small and giant lin-  
 344 ear dunes governed by the same dune growth mechanism (elongating mode).  
 345 Figure 9 shows how the orientations for the small and giant dunes can be

346 derived from the locally measured and regionally predicted winds respectively  
 347 (red arrows in Fig. 9). These predictions require to specify the threshold of  
 348 aeolian sand transport. Importantly, its value (a shear velocity estimated at  
 349  $u_{th} \simeq 0.15 \text{ m s}^{-1}$ ) can be reached in periods during which winds are deflected  
 350 (recall that the stronger winds, responsible for most of the sediment transport  
 351 and associated dune morphodynamics, are not deflected – see Fig. 6). The  
 352 feedback of the giant dunes on the wind described in this study, through wind  
 353 deflection and attenuation, thus provides a potential explanation for the exis-  
 354 tence of these small linear dunes elongating across the interdune, a dynamic  
 355 which has remained unresolved to date. These crossing dunes could provide  
 356 additional constraints for the inference of local winds from bedforms, similarly  
 357 to that currently performed on Mars using ripple orientations (Liu and Zim-  
 358 belman 2015; Hood et al. 2021). Further work is needed to investigate these  
 359 processes in more detail, including measurements of sediment transport and  
 360 flow on the top of dunes.

361 This study presents the evidence that wind flow patterns around giant  
 362 dunes are influenced by the atmospheric boundary layer, particularly during  
 363 nocturnal conditions. However, we do not address here the question of the  
 364 limitation of their pattern coarsening, and leave open the debate as to whether  
 365 the size of giant dunes is controlled by the depth of this layer (Andreotti et al.  
 366 2009), in contrast to sediment supply limited and ever-slower growth with  
 367 size (Werner and Kocurek 1999; Gunn et al. 2021a). More field evidence is  
 368 definitively needed from additional dune fields, but this mechanism would  
 369 allow for the inference of the ABL depth from giant bedform wavelengths  
 370 where measurements are not feasible or available, such as Titan (Lorenz et al.  
 371 2010).

372 To conclude on conditions under which the ERA5-Land reanalysis data can  
 373 reliably be used to study dune morphodynamics, we summarise the compari-  
 374 son of local (direct measurements) and regional (climate reanalysis) wind data  
 375 as follows. In flat areas, the agreement between the two confirms the ability of  
 376 the ERA5-Land climate reanalysis to predict the wind regime down to scales  
 377  $\sim 10 \text{ km}$ , i.e the model grid. When smaller scale topographies are present  
 378 (giant dunes in our case), locally measured winds can significantly differ from  
 379 the regionally predicted ones. This is the case when the disturbances induced  
 380 by the dunes interact with the lower part of the ABL vertical structure, which  
 381 presents circadian variations. During the day, when the capping layer is typi-  
 382 cally high, this interaction is small, and the ERA5-Land predictions are also  
 383 quantitatively consistent with the local data. During the night, however, the  
 384 presence of a shallow atmospheric boundary layer induces a strong confine-  
 385 ment of the flow, and is associated with large wind deflection by the dunes.  
 386 Importantly, we find that this effect can be counterbalanced for large wind  
 387 velocities, which are capable of deforming the capping layer, thus decreasing  
 388 the influence of the confinement.

389 The theoretical computation of the wind disturbances induced by sinu-  
 390 soidal ridges under flow confinement has been performed in the linear limit  
 391 (Andreotti et al. 2009, 2012), i.e. when the aspect ratio of these ridges is small

( $k\xi_0 \ll 1$ ). These models are able to qualitatively reproduce the observed wind deflection (Appendix 1, Online Resource Figs. S11 and S13), and thus provide the physical support for the interpretation we propose here based on hydrodynamic regimes. However, these models cannot quantitatively predict the magnitude of our observations, probably due to the presence of expected non-linearities in high confinement situations linked to strong flow modulations. Besides, these linear calculations only predict wind attenuation in the interdune, in contrast with the observed enhanced velocities associated with particular evening winds from the South during the period October-March (Online Resource Fig. S12). Some other models predict different spatial flow structures in response to a modulated topography, such as lee waves and rotors (Baines 1995; Vosper 2004). However, our measurements are located at a single point in the interdune, and we are thus unable to explore these types of responses. Data at different places along and across the ridges are needed to investigate and possibly map such flow structures, and for further comparisons with the models.

**Acknowledgements** We would like to acknowledge the contributors of the following open-source python libraries, Matplotlib (Hunter 2007), Numpy (Harris et al. 2020) and Scipy (Virtanen et al. 2020), which provide an incredibly efficient ecosystem allowing scientific research in Python. We also thank B. Andreotti and A. Gunn for useful discussions.

All data used in this study can be found in Gadali et al. (2022). Note that it contains modified Copernicus Climate Change Service Information (2021). Neither the European Commission nor ECMWF is responsible for any use that may be made of the Copernicus Information or Data it contains. Documented codes used in this study to analyse this data are available at <https://github.com/Cgadali/GiantDunes> (will be made public upon acceptance of this manuscript for publication).

Multiple grants have supported the collection of wind data through visits to the four sites between 2013 and 2020 (John Fell Oxford University Press (OUP) Research Fund (121/474); National Geographic (CP-029R-17); Natural Environment Research Council UK (NE/R010196/1 and NE/H021841/1 NSFGEO-NERC); Southampton Marine and Maritime Institute SMMI EPSRC-GCRF UK), along with research permits (1978/2014, 2140/2016, 2304/2017, 2308/2017, RPIV00022018, RPIV0052018, RPIV00230218). The authors are very grateful for support from Etosha National Park (especially Shyane Kötting, Boas Erckie, Pierre du Preez, Claudine Cloete, Immanuel Kapofi, Wilferd Versfeld, and Werner Kilian), Gobabeb Namib Research Institute (Gillian Maggs-Kölling and Eugene Marais), The Skeleton Coast National Park (Joshua Kazeurua). Various researchers and desert enthusiasts have assisted with instruments and the logistics of expeditions, especially Mary Seely for expert guidance at the North Sand Sea site.

Finally, we acknowledge financial support from the Laboratoire d'Excellence UnivEarthS Grant ANR-10-LABX-0023, the Initiative d'Excellence Université de Paris Grant ANR-18-IDEX-0001, the French National Research Agency Grants ANR-17-CE01-0014/SONO and the National Science Center of Poland Grant 2016/23/B/ST10/01700.

#### Appendix 1: Linear theory of wind response to topographic perturbation

Following the work of Fourrière et al. (2010), Andreotti et al. (2012) and Andreotti et al. (2009), we briefly describe in this appendix the framework for the linear response of a turbulent flow to a topographic perturbation of

<sup>439</sup> small aspect ratio. As a general bed elevation can be decomposed into Fourier  
<sup>440</sup> modes, we focus here on a sinusoidal topography:

$$\xi = \xi_0 \cos [k (\cos(\alpha)y - \sin(\alpha)x)], \quad (3)$$

<sup>441</sup> which is also a good approximation for the giant dunes observed in the North  
<sup>442</sup> Sand Sea and South Sand Sea Station (Fig. 2 and Online Resource Fig. S4).  
<sup>443</sup> Here,  $x$  and  $y$  are the streamwise and spanwise coordinates,  $k = 2\pi/\lambda$  the  
<sup>444</sup> wavenumber of the sinusoidal perturbation,  $\alpha$  its crest orientation with respect  
<sup>445</sup> to the  $x$ -direction (anticlockwise) and  $\xi_0$  its amplitude. The two components  
<sup>446</sup> of the basal shear stress  $\tau = \rho_0 u_* \mathbf{u}_*$ , constant in the flat bottom reference  
<sup>447</sup> case, can then be generically written as:

$$\tau_x = \tau_0 \left( 1 + k\xi_0 \sqrt{\mathcal{A}_x^2 + \mathcal{B}_x^2} \cos [k (\cos(\alpha)y - \sin(\alpha)x) + \phi_x] \right), \quad (4)$$

$$\tau_y = \tau_0 k\xi_0 \sqrt{\mathcal{A}_y^2 + \mathcal{B}_y^2} \cos [k (\cos(\alpha)y - \sin(\alpha)x) + \phi_y], \quad (5)$$

<sup>448</sup> where  $\tau_0$  is the reference basal shear stress on a flat bed. We have defined  
<sup>449</sup> the phase  $\phi_{x,y} = \tan^{-1}(\mathcal{B}_{x,y}/\mathcal{A}_{x,y})$  from the in-phase and in-quadrature hy-  
<sup>450</sup> drodynamical coefficients  $\mathcal{A}_{x,y}$  and  $\mathcal{B}_{x,y}$ . They are functions of  $k$  and of the  
<sup>451</sup> flow conditions, i.e the bottom roughness, the vertical flow structure and the  
<sup>452</sup> incident flow direction, and the theoretical framework developed in the above  
<sup>453</sup> cited papers proposes methods to compute them in the linear regime.

<sup>454</sup> Following Andreotti et al. (2012), the effect of the incident wind direction  
<sup>455</sup> can be approximated by the following expressions:

$$\mathcal{A}_x = \mathcal{A}_0 \sin^2 \alpha, \quad (6)$$

$$\mathcal{B}_x = \mathcal{B}_0 \sin^2 \alpha, \quad (7)$$

$$\mathcal{A}_y = -\frac{1}{2} \mathcal{A}_0 \cos \alpha \sin \alpha, \quad (8)$$

$$\mathcal{B}_y = -\frac{1}{2} \mathcal{B}_0 \cos \alpha \sin \alpha, \quad (9)$$

<sup>456</sup> where  $\mathcal{A}_0$  and  $\mathcal{B}_0$  are now two coefficients independent of the dune orienta-  
<sup>457</sup> tion  $\alpha$ , corresponding to the transverse case ( $\alpha = 90^\circ$ ). In the case of a fully  
<sup>458</sup> turbulent boundary layer capped by a stratified atmosphere, these coefficients  
<sup>459</sup> depend on  $kH$ ,  $kz_0$ ,  $\mathcal{F}$  and  $\mathcal{F}_I$  (Andreotti et al. 2009). For their computation,  
<sup>460</sup> we assume here a constant hydrodynamic roughness  $z_0 \simeq 1$  mm (Online Re-  
<sup>461</sup> source section 1). For the considered giant dunes, this leads to  $kz_0 \simeq 2 \cdot 10^{-6}$ ,  
<sup>462</sup> as their wavelength is  $\lambda \simeq 2.4$  km (or  $k \simeq 2 \cdot 10^{-3}$  m $^{-1}$ ). Values of  $z_0$  extracted  
<sup>463</sup> from field data indeed typically fall between 0.1 mm and 10 mm (Sherman and  
<sup>464</sup> Farrell 2008; Field and Pelletier 2018). Importantly,  $\mathcal{A}_0$  and  $\mathcal{B}_0$  do not vary  
<sup>465</sup> much in the corresponding range of  $kz_0$  (Fourrière et al. 2010), and the results  
<sup>466</sup> presented here are robust with respect to this choice.

<sup>467</sup> With capping layer height and Froude numbers computed from the ERA5-  
<sup>468</sup> Land time series, the corresponding  $\mathcal{A}_0$  and  $\mathcal{B}_0$  can be deduced, as displayed  
<sup>469</sup> in Online Resource Fig. S13. Interestingly, it shows similar regimes as in the

470 diagrams of Fig. 8 and Online Resource Fig. S11a,b, supporting the underlying  
 471 physics. However, the agreement is qualitative only. Further, the linearity  
 472 assumption of the theoretical framework requires  $(|\tau| - \tau_0)/\tau_0 \ll 1$ , which  
 473 translates into  $k\xi\sqrt{\mathcal{A}_0^2 + \mathcal{B}_0^2} \ll 1$ . In our case, the giant dune morphology  
 474 gives  $k\xi_0 \simeq 0.1$ , which means that one quits the regime of validity of the  
 475 linear theory when the coefficient modulus  $\sqrt{\mathcal{A}_0^2 + \mathcal{B}_0^2}$  becomes larger than a  
 476 few units. In accordance with the theoretical expectations, these coefficients  
 477 present values on the order of unity ( $\mathcal{A}_0 \simeq 3$  and  $\mathcal{B}_0 \simeq 1$ ) in unconfined sit-  
 478 uations (Claudin et al. 2013; Lü et al. 2021). In contrast and as illustrated  
 479 in Online Resource Fig. S13a,b, larger values are predicted in case of strong  
 480 confinement, which does not allow us to proceed to further quantitative com-  
 481 parison with the data.

482 Finally, the linear model is also able to reproduce the enhancement of the  
 483 flow deflection over the sinusoidal ridges when  $\sqrt{\mathcal{A}_0^2 + \mathcal{B}_0^2}$  is increased (Online  
 484 Resource Fig. S13). Here, using  $k\xi_0 \simeq 0.1$  to be representative of the amplitude  
 485 of the giant dunes at the North Sand Sea station, the coefficient modulus is  
 486 bounded to 10.

## 487 Appendix 2: Sediment transport and dune morphodynamics

488 We summarise in this appendix the sediment transport and dune morphody-  
 489 namics theoretical framework leading to the prediction of sand fluxes and dune  
 490 orientations from wind data.

491 *Sediment transport* — The prediction of sand fluxes from wind data has been  
 492 a long standing issue in aeolian geomorphological studies (Fryberger and Dean  
 493 1979; Pearce and Walker 2005; Sherman and Li 2012; Shen et al. 2019). Based  
 494 on laboratory studies in wind tunnels (Rasmussen et al. 1996; Iversen and  
 495 Rasmussen 1999; Creyssels et al. 2009; Ho et al. 2011), as well as physical  
 496 considerations (Ungar and Haff 1987; Andreotti 2004; Durán et al. 2011; Pähzt  
 497 and Durán 2020), it has been shown that the steady saturated saltation flux  
 498 over a flat sand bed depends linearly on the shear stress:

$$\frac{q_{\text{sat}}}{Q} = \Omega \sqrt{\Theta_{\text{th}}} (\Theta - \Theta_{\text{th}}), \quad (10)$$

499 where  $\Omega$  is a proportionality constant,  $Q = d\sqrt{(\rho_s - \rho_0)gd/\rho_0}$  is a character-  
 500 istic flux,  $\Theta = \rho_0 u_*^2 / (\rho_s - \rho_0)gd$  the Shields number, and  $\Theta_{\text{th}}$  its threshold  
 501 value below which saltation vanishes.  $\rho_s = 2.6 \text{ g cm}^{-3}$  and  $d = 180 \mu\text{m}$  are  
 502 the grain density and diameter, and  $g$  is the gravitational acceleration. The  
 503 shear velocity, and consequently the Shields number as well as the sediment  
 504 flux, are time dependent.

505 Recently, Pähzt and Durán (2020) suggested an additional quadratic term  
 506 in Shields to account for grain-grain interactions within the transport layer at  
 507 strong wind velocities:

$$\frac{q_{\text{sat}, t}}{Q} = \frac{2\sqrt{\Theta_{\text{th}}}}{\kappa\mu} (\Theta - \Theta_{\text{th}}) \left( 1 + \frac{C_M}{\mu} [\Theta - \Theta_{\text{th}}] \right), \quad (11)$$

508 where  $\kappa = 0.4$  is the von Kármán constant,  $C_M \simeq 1.7$  a constant and  $\mu \simeq 0.6$  is  
 509 a friction coefficient, taken to be the avalanche slope of the granular material.  
 510 The fit of this law to the experimental data of Creyssels et al. (2009) and Ho  
 511 et al. (2011) gives  $\Theta_{\text{th}} = 0.0035$ . The fit of Eq. 10 on these same data similarly  
 512 gives  $\Omega \simeq 8$  and  $\Theta_{\text{th}} = 0.005$ . The sand flux angular distributions and the  
 513 dune orientations in Fig. 9 are calculated using this law (11). We have checked  
 514 that using the ordinary linear relationship (10) instead does not change the  
 515 predicted dune orientations by more than a few degrees.

516 *Dune orientations* — Dune orientations are predicted with the dimensional  
 517 model of Courrech du Pont et al. (2014), from the sand flux time series com-  
 518 puted with the above transport law. Two orientations are possible depending  
 519 on the mechanism dominating the dune growth: elongation or bed instabil-  
 520 ity. The orientation  $\alpha$  corresponding the bed instability is then the one that  
 521 maximises the following growth rate (Rubin and Hunter 1987):

$$\sigma \propto \frac{1}{H_d W_d T} \int_0^T q_{\text{crest}} |\sin(\theta - \alpha)| dt, \quad (12)$$

522 where  $\theta$  is the wind orientation measured with respect to the same reference  
 523 as  $\alpha$ , and  $H_d$  and  $W_d$  are dimensional constants respectively representing the  
 524 dune height and width. The integral runs over a time  $T$ , which must be repre-  
 525 sentative of the characteristic period of the wind regime. The flux at the crest  
 526 is expressed as:

$$q_{\text{crest}} = q_{\text{sat}} [1 + \gamma |\sin(\theta - \alpha)|], \quad (13)$$

527 where the flux-up ratio  $\gamma$  has been calibrated to 1.6 using field studies, under-  
 528 water laboratory experiments and numerical simulations. Predictions of the  
 529 linear analysis of Gadal et al. (2019) and Delorme et al. (2020) give similar  
 530 results.

531 Similarly, the dune orientation corresponding to the elongation mechanism  
 532 is the one that verifies:

$$\tan(\alpha) = \frac{\langle q_{\text{crest}}(\alpha) e_\theta \rangle \cdot e_{WE}}{\langle q_{\text{crest}}(\alpha) e_\theta \rangle \cdot e_{SN}}, \quad (14)$$

533 where  $\langle \cdot \rangle$  denotes a vectorial time average. The unitary vectors  $e_{WE}$ ,  $e_{SN}$  and  
 534  $e_\theta$  are in the West-East, South-North and wind directions, respectively.

535 The resulting computed dune orientations, blue and red arrows in Fig. 9,  
 536 then depend on a certain number of parameters (grain properties, flux-up ratio,  
 537 etc.), for which we take typical values for aeolian sandy deserts. Due to the lack  
 538 of measurements in the studied places, some uncertainties can be expected. We  
 539 therefore run a sensitivity test by calculating the dune orientations for grain  
 540 diameters ranging from  $100 \mu\text{m}$  to  $400 \mu\text{m}$  and for a speed-up ratio between  
 541 0.1 and 10 (wedges in Fig. 9).

---

**542 References**

- 543 Andreotti B (2004) A two-species model of aeolian sand transport. *J Fluid  
544 Mech* 510:47–70
- 545 Andreotti B, Claudin P, Douady S (2002) Selection of dune shapes and veloc-  
546 ities part 1: Dynamics of sand, wind and barchans. *The European Physical  
547 Journal B-Condensed Matter and Complex Systems* 28:321–339
- 548 Andreotti B, Fourrière A, Ould-Kaddour F, Murray B, Claudin P (2009) Gi-  
549 ant aeolian dune size determined by the average depth of the atmospheric  
550 boundary layer. *Nature* 457:1120–1123
- 551 Andreotti B, Claudin P, Devauchelle O, Durán O, Fourrière A (2012) Bedforms  
552 in a turbulent stream: ripples, chevrons and antidunes. *J Fluid Mech* 690:94–  
553 128
- 554 Ashkenazy Y, Yizhaq H, Tsoar H (2012) Sand dune mobility under climate  
555 change in the kalahari and australian deserts. *Climatic Change* 112:901–923
- 556 Baddock M, Livingstone I, Wiggs G (2007) The geomorphological significance  
557 of airflow patterns in transverse dune interdunes. *Geomorphology* 87:322–  
558 336
- 559 Bagnold RA (1941) *The Physics of Blown Sand and Desert Dunes*. London :  
560 Methuen : Chapman & Hall
- 561 Baines PG (1995) Topographic effects in stratified flows. Cambridge university  
562 press
- 563 Bauer BO, Sherman DJ, Wolcott JF (1992) Sources of uncertainty in shear  
564 stress and roughness length estimates derived from velocity profiles. *The  
565 Professional Geographer* 44:453–464
- 566 Belcher S, Hunt J (1998) Turbulent flow over hills and waves. *Annu Rev Fluid  
567 Mech* 30:507–538
- 568 Blumberg DG, Greeley R (1996) A comparison of general circulation model  
569 predictions to sand drift and dune orientations. *J Clim* 9:3248–3259
- 570 Bristow NR, Best J, Wiggs GFS, Nield JM, Baddock MC, Delorme P, Chris-  
571 tensen KT (2022) Topographic perturbation of turbulent boundary layers  
572 by low-angle, early-stage aeolian dunes. *Earth Surf Process Landf* n/a, DOI  
573 <https://doi.org/10.1002/esp.5326>
- 574 Brookfield M (1977) The origin of bounding surfaces in ancient aeolian sand-  
575 stones. *Sedimentology* 24:303–332
- 576 Brown S, Nickling WG, Gillies JA (2008) A wind tunnel examination of shear  
577 stress partitioning for an assortment of surface roughness distributions. *J  
578 Geophys Res* 113:F02S06
- 579 Chandler C, Radebaugh J, McBride J, Morris T, Narteau C, Arnold K, Lorenz  
580 R, Barnes J, Hayes A, Rodriguez S, Rittenour T (2022) Near-surface struc-  
581 ture of a large linear dune and an associated crossing dune of the northern  
582 namib sand sea from ground penetrating radar: Implications for the his-  
583 tory of large linear dunes on earth and titan. *Aeolian Research* 57:100813,  
584 DOI <https://doi.org/10.1016/j.aeolia.2022.100813>
- 585 Chang H, Simons D (1970) The bed configuration of straight sand-bed channels  
586 when flow is nearly critical. *J Fluid Mech* 42:491–495

- 587 Charru F, Andreotti B, Claudin P (2013) Sand ripples and dunes. *Annu Rev Fluid Mech* 45:469–493
- 588 Claudin P, Wiggs G, Andreotti B (2013) Field evidence for the upwind velocity shift at the crest of low dunes. *Boundary-Layer Meteorol* 148:195–206
- 589 Claudin P, Durán O, Andreotti B (2017) Dissolution instability and roughening transition. *J Fluid Mech* 832:R2
- 590 Claudin P, Louge M, Andreotti B (2021) Basal pressure variations induced by a turbulent flow over a wavy surface. *Frontiers in Physics* 9:682564
- 591 Colombini M (2004) Revisiting the linear theory of sand dune formation. *J Fluid Mech* 502:1–16
- 592 Courrech du Pont S (2015) Dune morphodynamics. *C R Phys* 16:118–138
- 593 Courrech du Pont S, Narteau C, Gao X (2014) Two modes for dune orientation. *Geology* 42:743–746
- 594 Creyssels M, Dupont P, El Mohtar AO, Valance A, Cantat I, Jenkins JT, Pasini JM, Rasmussen KR (2009) Saltating particles in a turbulent boundary layer: experiment and theory. *J Fluid Mech* 625:47–74
- 595 de Winter W, Donker J, Sterk G, Van Beem J, Ruessink G (2020) Regional versus local wind speed and direction at a narrow beach with a high and steep foredune. *Plos one* 15:e0226983
- 596 Dee DP, Uppala SM, Simmons AJ, Berrisford P, Poli P, Kobayashi S, Andrae U, Balmaseda M, Balsamo G, Bauer dP, et al. (2011) The era-interim re-analysis: Configuration and performance of the data assimilation system. *Q J R Meteorol Soc* 137:553–597
- 597 Delorme P, Wiggs G, Baddock M, Claudin P, Nield J, Valdez A (2020) Dune initiation in a bimodal wind regime. *J Geophys Res* 125:e2020JF005757
- 598 Durán O, Claudin P, Andreotti B (2011) On aeolian transport: Grain-scale interactions, dynamical mechanisms and scaling laws. *Aeolian Res* 3:243–270
- 599 Durran DR (1990) Mountain waves and downslope winds. In: *Atmospheric processes over complex terrain*, Springer, pp 59–81
- 600 Dyer A (1974) A review of flux-profile relationships. *Boundary-Layer Meteorol* 7:363–372
- 601 Ewing RC, Kocurek G, Lake LW (2006) Pattern analysis of dune-field parameters. *Earth Surf Process Landf* 31:1176–1191
- 602 Farr TG, Rosen PA, Caro E, Crippen R, Duren R, Hensley S, Kobrick M, Paller M, Rodriguez E, Roth L, et al. (2007) The shuttle radar topography mission. *Rev Geophys* 45
- 603 Fernando H, Mann J, Palma J, Lundquist JK, Barthelmie RJ, Belo-Pereira M, Brown W, Chow F, Gerz T, Hocut C, et al. (2019) The perdigão: Peering into microscale details of mountain winds. *Bull Am Meteorol Soc* 100:799–819
- 604 Field JP, Pelletier JD (2018) Controls on the aerodynamic roughness length and the grain-size dependence of aeolian sediment transport. *Earth Surf Process Landf* 43:2616–2626
- 605 Finnigan J, Raupach M, Bradley E, Aldis G (1990) A wind tunnel study of turbulent flow over a two-dimensional ridge. *Boundary-Layer Meteorol*

- 633 50:277–317
- 634 Finnigan J, Ayotte K, Harman I, Katul G, Oldroyd H, Patton E, Poggi D,  
635 Ross A, Taylor P (2020) Boundary-layer flow over complex topography.  
Boundary-Layer Meteorol 177:247–313
- 637 Flack K, Schultz M (2010) Review of hydraulic roughness scales in the fully  
638 rough regime. Journal of Fluids Engineering 132:041203
- 639 Fourrière A, Claudin P, Andreotti B (2010) Bedforms in a turbulent stream:  
640 formation of ripples by primary linear instability and of dunes by nonlinear  
641 pattern coarsening. J Fluid Mech 649:287–328
- 642 Frederick KA, Hanratty TJ (1988) Velocity measurements for a turbulent non-  
643 separated flow over solid waves. Exp Fluids 6:477–486
- 644 Fryberger SG, Dean G (1979) Dune forms and wind regime. A study of global  
645 sand seas 1052:137–169
- 646 Gadal C, Narteau C, Courrech Du Pont S, Rozier O, Claudin P (2019) Incip-  
647 ient bedforms in a bidirectional wind regime. J Fluid Mech 862:490–516
- 648 Gadal C, Narteau C, Courrech du Pont S, Rozier O, Claudin P (2020) Peri-  
649 odicity in fields of elongating dunes. Geology 48:343–347
- 650 Gadal C, Delorme P, Narteau C, Wiggs G, Baddock M, Nield JM, Claudin  
651 P (2022) Data used in 'Local wind regime induced by giant linear dunes:  
652 comparison of ERA5-Land re-analysis with surface measurements'. DOI  
653 10.5281/zenodo.6343138
- 654 Garratt JR (1994) The atmospheric boundary layer. Earth-Science Reviews  
655 37:89–134
- 656 Garvey B, Castro IP, Wiggs G, Bullard J (2005) Measurements of flows over  
657 isolated valleys. Boundary-Layer Meteorol 117:417–446
- 658 Gong W, Ibbetson A (1989) A wind tunnel study of turbulent flow over model  
659 hills. Boundary-Layer Meteorol 49:113–148
- 660 Gong W, Taylor P, Dörnbrack A (1996) Turbulent boundary-layer flow over  
661 fixed aerodynamically rough two-dimensional sinusoidal waves. J Fluid Mech  
662 312:1–37
- 663 Guérin A, Derr J, Du Pont SC, Berhanu M (2020) Streamwise dissolution  
664 patterns created by a flowing water film. Phys Rev Lett 125:194502
- 665 Gunn A, Casasanta G, Di Liberto L, Falcini F, Lancaster N,  
666 Jerolmack DJ (2021a) What sets aeolian dune height? DOI  
667 <https://doi.org/10.31223/X5QG8S>
- 668 Gunn A, Wanker M, Lancaster N, Edmonds D, Ewing R, Jerolmack  
669 D (2021b) Circadian rhythm of dune-field activity. Geophys Res Lett  
670 48:e2020GL090924
- 671 Harris CR, Millman KJ, van der Walt SJ, Gommers R, Virtanen P, Cournapeau  
672 D, Wieser E, Taylor J, Berg S, Smith NJ, et al. (2020) Array program-  
673 ming with numpy. Nature 585:357–362
- 674 Havholm KG, Kocurek G (1988) A preliminary study of the dynamics of a  
675 modern draa, algodones, southeastern california, usa. Sedimentology 35:649–  
669
- 677 Hersbach H, Bell B, Berrisford P, Hirahara S, Horányi A, Muñoz-Sabater J,  
678 Nicolas J, Peubey C, Radu R, Schepers D, et al. (2020) The era5 global

- 679 reanalysis. *Q J R Meteorol Soc* 146:1999–2049
- 680 Hesp P, Illenberger W, Rust I, McLachlan A, Hyde R (1989) Some aspects of  
681 transgressive dunefield and transverse dune geomorphology and dynamics,  
682 south coast, south africa. *Zeitschrift fur Geomorphologie*, Supplementband  
683 73:111–123
- 684 Hesp PA, Hastings K (1998) Width, height and slope relationships and aero-  
685 dynamic maintenance of barchans. *Geomorphology* 22:193–204
- 686 Hesp PA, Smyth TAG, Nielsen P, Walker IJ, Bauer BO, Davidson-Arnott R  
687 (2015) Flow deflection over a foredune. *Geomorphology* 230:64–74
- 688 Ho TD, Valance A, Dupont P, Ould El Moctar A, Tuan Duc H, Valance A,  
689 Dupont P, Ould El Moctar A (2011) Scaling laws in aeolian sand transport.  
690 *Phys Rev Lett* 106:4–7
- 691 Hood DR, Ewing RC, Roback KP, Runyon K, Avouac JP, McEnroe M (2021)  
692 Inferring airflow across martian dunes from ripple patterns and dynamics.  
693 *Frontiers in Earth Science* 9:702828
- 694 Howard AD (1977) Effect of slope on the threshold of motion and its applica-  
695 tion to orientation of wind ripples. *Geological Society of America Bulletin*  
696 88:853–856
- 697 Hu Z, Gao X, Lei J, Zhou N (2021) Geomorphology of aeolian dunes in the  
698 western sahara desert. *Geomorphology* 392:107916
- 699 Hunt J, Leibovich S, Richards K (1988) Turbulent shear flows over low hills.  
700 *Q J R Meteorol Soc* 114:1435–1470
- 701 Hunt JCR, Vilenski GG, Johnson ER (2006) Stratified separated flow around  
702 a mountain with an inversion layer below the mountain top. *J Fluid Mech*  
703 556:105–119
- 704 Hunter JD (2007) Matplotlib: A 2d graphics environment. *Computing in sci-  
705 ence & engineering* 9:90–95
- 706 Hunter RE, Richmond BM, Alpha TR (1983) Storm-controlled oblique dunes  
707 of the oregon coast. *Geol Soc America Bull* 94:1450–1465
- 708 Iversen JD, Rasmussen KR (1999) The effect of wind speed and bed slope on  
709 sand transport. *Sedimentology* 46:723–731
- 710 Jackson PS, Hunt JCR (1975) Turbulent wind flow over a low hill. *Q J R  
711 Meteorol Soc* 101:929–955
- 712 Jiang Q (2014) Applicability of reduced-gravity shallow-water theory to atmo-  
713 pheric flow over topography. *J Atmos Sci* 71:1460–1479
- 714 Jolivet M, Braucher R, Dovchintseren D, Hocquet S, Schmitt J, ASTER Team  
715 (2021) Erosion around a large-scale topographic high in a semi-arid sedimen-  
716 tary basin: Interactions between fluvial erosion, aeolian erosion and aeolian  
717 transport. *Geomorphology* 386:107747
- 718 Kennedy JF (1963) The mechanics of dunes and antidunes in erodible-bed  
719 channels. *J Fluid Mech* 16:521–544
- 720 Kim HG, Patel VC, Lee CM (2000) Numerical simulation of wind flow over  
721 hilly terrain. *J Wind Eng Ind Aerodyn* 87:45–60
- 722 Kroy K, Sauermann G, Herrmann HJ (2002) Minimal model for aeolian sand  
723 dunes. *Phys Rev E* 66:031302

- 724 Lancaster J, Lancaster N, Seely M (1984) Climate of the central namib desert.  
725 Madoqua 1984:5–61
- 726 Lancaster N (1985) Winds and sand movements in the namib sand sea. Earth  
727 Surf Process Landf 10:607–619
- 728 Lancaster N, Nickling W, Neuman CM, Wyatt V (1996) Sediment flux and  
729 airflow on the stoss slope of a barchan dune. Geomorphology 17:55–62
- 730 Lewis HW, Mobbs SD, Lehning M (2008) Observations of cross-ridge flows  
731 across steep terrain. Q J R Meteorol Soc 134:801–816
- 732 Liu ZYC, Zimbelman JR (2015) Recent near-surface wind directions inferred  
733 from mapping sand ripples on martian dunes. Icarus 261:169–181
- 734 Livingstone I, Warren A (2019) Aeolian geomorphology: a new introduction.  
735 Wiley
- 736 Livingstone I, Bristow C, Bryant RG, Bullard J, White K, Wiggs GFS, Baas  
737 ACW, Bateman MD, Thomas DSG (2010) The namib sand sea digital  
738 database of aeolian dunes and key forcing variables. Aeolian Res 2:93–104
- 739 Lorenz R, Claudin P, Andreotti B, Radebaugh J, Tokano T (2010) A 3 km  
740 atmospheric boundary layer on titan indicated by dune spacing and huygens  
741 data. Icarus 205:719–721
- 742 Lü P, Narteau C, Dong Z, Rozier O, Du Pont SC (2017) Unravelling raked  
743 linear dunes to explain the coexistence of bedforms in complex dunefields.  
744 Nature communications 8:1–9
- 745 Lü P, Narteau C, Dong Z, Claudin P, Rodriguez S, An Z, Fernandez-Cascales  
746 L, Gadale C, Courrech du Pont S (2021) Direct validation of dune instability  
747 theory. Proceedings of the National Academy of Sciences 118
- 748 Mason P, Sykes R (1979) Flow over an isolated hill of moderate slope. Q J R  
749 Meteorol Soc 105:383–395
- 750 McKenna Neuman C, Lancaster N, Nickling WG (1997) Relations between  
751 dune morphology, air flow, and sediment flux on reversing dunes, Silver Peak,  
752 Nevada. Sedimentology 44:1103–1111, DOI 10.1046/j.1365-3091.1997.d01-  
753 61.x
- 754 Mizumura K (1995) Free-surface profile of open-channel flow with wavy bound-  
755 ary. J Hydraul Eng 121:533–539
- 756 Monin AS, Obukhov AM (1954) Basic laws of turbulent mixing in the surface  
757 layer of the atmosphere. Contrib Geophys Inst Acad Sci USSR 151:e187
- 758 Mulligan KR (1988) Velocity profiles measured on the windward slope of a  
759 transverse dune. Earth Surf Process Landf 13:573–582
- 760 Muñoz-Sabater J, Dutra E, Agustí-Panareda A, Albergel C, Arduini G, Bal-  
761 samo G, Boussetta S, Choulga M, Harrigan S, Hersbach H, et al. (2021)  
762 Era5-land: A state-of-the-art global reanalysis dataset for land applications.  
763 Earth Syst Sci Data 13:4349–4383
- 764 Nield JM, King J, Wiggs GFS, Leyland J, Bryant RG, Chiverrell RC, Darby  
765 SE, Eckhardt FD, Thomas DSG, Vircavs LH, Washington R (2014) Esti-  
766 mating aerodynamic roughness over complex surface terrain. J Geophys Res  
767 118:12948–12961
- 768 Nield JM, Wiggs GF, Baddock MC, Hipondoka MH (2017) Coupling leeside  
769 rainfall to avalanche characteristics in aeolian dune dynamics. Geology

- 770 45:271–274
- 771 Pähzt T, Durán O (2020) Unification of aeolian and fluvial sediment transport  
772 rate from granular physics. *Phys Rev Lett* 124:168001
- 773 Pearce KI, Walker IJ (2005) Frequency and magnitude biases in the 'Fryberger'  
774 model, with implications for characterizing geomorphically effective winds.  
775 *Geomorphology* 68:39–55
- 776 Pelletier JD, Field JP (2016) Predicting the roughness length of turbulent flows  
777 over landscapes with multi-scale microtopography. *Earth Surface Dynamics*  
778 4:391–405
- 779 Poggi D, Katul G, Albertson J, Ridolfi L (2007) An experimental investigation  
780 of turbulent flows over a hilly surface. *Phys Fluids* 19:036601
- 781 Rasmussen KR (1989) Some aspects of flow over coastal dunes. *Proceedings of*  
782 *the Royal Society of Edinburgh, Section B: Biological Sciences* 96:129–147
- 783 Rasmussen KR, Iversen JD, Rautaheimo P (1996) Saltation and wind flow  
784 interaction in a variable slope wind tunnel. *Geomorphology* 17:19–28
- 785 Raupach M (1992) Drag and drag partition on rough surfaces. *Boundary-Layer*  
786 *Meteorol* 60:375–395
- 787 Rubin DM, Hunter RE (1987) Bedform alignment in directionally varying  
788 flows. *Science* 237:276–278
- 789 Runyon K, Bridges N, Ayoub F, Newman C, Quade J (2017) An integrated  
790 model for dune morphology and sand fluxes on mars. *Earth and Planetary*  
791 *Science Letters* 457:204–212
- 792 Sauermann G, Andrade Jr J, Maia L, Costa U, Araújo A, Herrmann H  
793 (2003) Wind velocity and sand transport on a barchan dune. *Geomorphology*  
794 54:245–255
- 795 Seidel DJ, Zhang Y, Beljaars A, Golaz JC, Jacobson AR, Medeiros B (2012)  
796 Climatology of the planetary boundary layer over the continental united  
797 states and europe. *J Geophys Res* 117:D17106
- 798 Shao Y (2008) Physics and modelling of wind erosion, vol 37. Springer Science  
799 & Business Media
- 800 Shen Y, Zhang C, Huang X, Wang X, Cen S (2019) The effect of wind speed  
801 averaging time on sand transport estimates. *Catena* 175:286–293
- 802 Sheridan PF, Vosper SB (2006) A flow regime diagram for forecasting lee  
803 waves, rotors and downslope winds. *Meteorol Appl* 13:179–195
- 804 Sherman CA (1978) A mass-consistent model for wind fields over complex  
805 terrain. *J Appl Meteorol Clim* 17:312–319
- 806 Sherman D, Farrell E (2008) Aerodynamic roughness lengths over movable  
807 beds: Comparison of wind tunnel and field data. *J Geophys Res* 113:1–10
- 808 Sherman DJ, Li B (2012) Predicting aeolian sand transport rates: A reevalu-  
809 ation of models. *Aeolian Res* 3:371–378
- 810 Smith AB, Jackson DWT, Cooper JAG (2017) Three-dimensional airflow and  
811 sediment transport patterns over barchan dunes. *Geomorphology* 278:28–42
- 812 Song Q, Gao X, Lei J, Li S (2019) Spatial distribution of sand dunes and their  
813 relationship with fluvial systems on the southern margin of the taklimakan  
814 desert, china. *Geomatics, Natural Hazards and Risk* 10:2408–2428

- 815 Spalding DB (1961) A single formula for the law of the wall. *Journal of Applied  
816 Mechanics* 28:455–458
- 817 Stull R (2006) 9 - the atmospheric boundary layer. In: Wallace JM, Hobbs PV  
818 (eds) *Atmospheric Science* (Second Edition), second edition edn, Academic  
819 Press, San Diego, pp 375–417
- 820 Stull RB (1988) An introduction to boundary layer meteorology, vol 13.  
821 Springer Science & Business Media
- 822 Sullivan PP, McWilliams JC (2010) Dynamics of winds and currents coupled  
823 to surface waves. *Annu Rev Fluid Mech* 42:19–42
- 824 Sweet M, Kocurek G (1990) An empirical model of aeolian dune lee-face air-  
825 flow. *Sedimentology* 37:1023–1038
- 826 Sykes RI (1980) An asymptotic theory of incompressible turbulent boundary-  
827 layer flow over a small hump. *J Fluid Mech* 101:647–670
- 828 Taylor P, Teunissen H (1987) The Askervein hill project: overview and back-  
829 ground data. *Boundary-Layer Meteorol* 39:15–39
- 830 Taylor P, Mason P, Bradley E (1987) Boundary-layer flow over low hills.  
831 *Boundary-Layer Meteorol* 39:107–132
- 832 Tsoar H, Yaalon DH (1983) Deflection of sand movement on a sinuous longi-  
833 tudinal (seif) dune: use of fluorescent dye as tracer. *Sedimentary Geology*  
834 36:25–39
- 835 Ungar JE, Haff PK (1987) Steady state saltation in air. *Sedimentology* 34:289–  
836 299
- 837 Unsworth C, Parsons D, Hardy R, Reesink A, Best J, Ashworth P, Keevil G  
838 (2018) The impact of nonequilibrium flow on the structure of turbulence  
839 over river dunes. *Water Resour Res* 54:6566–6584
- 840 Uppala SM, Källberg P, Simmons AJ, Andrae U, Bechtold VDC, Fiorino M,  
841 Gibson J, Haseler J, Hernandez A, Kelly G, et al. (2005) The era-40 re-  
842 analysis. *Q J R Meteorol Soc* 131:2961–3012
- 843 Valance A, Rasmussen K, Ould El Moctar A, Dupont P (2015) The physics  
844 of aeolian sand transport. *C R Phys* 16:1–13
- 845 Venditti JG, Best JL, Church M, Hardy RJ (2013) Coherent Flow Structures  
846 at Earth's Surface. John Wiley & Sons
- 847 Virtanen P, Gommers R, Oliphant TE, Haberland M, Reddy T, Cournapeau  
848 D, Burovski E, Peterson P, Weckesser W, Bright J, et al. (2020) Scipy 1.0:  
849 fundamental algorithms for scientific computing in python. *Nature methods*  
850 17:261–272
- 851 Vogelegang D, Holtslag A (1996) Evaluation and model impacts of alternative  
852 boundary-layer height formulations. *Boundary-Layer Meteorol* 81:245–269
- 853 Vosper SB (2004) Inversion effects on mountain lee waves. *Q J R Meteorol Soc*  
854 130:1723–1748
- 855 Walker I, Davidson-Arnott R, Bauer B, Hesp P, Delgado-Fernandez I, Oller-  
856 head J, Smyth T (2017) Scale-dependent perspectives on the geomorphology  
857 and evolution of beach-dune systems. *Earth-Science Review* 171:220–253
- 858 Walker IJ, Nickling WG (2002) Dynamics of secondary airflow and sediment  
859 transport over and in the lee of transverse dunes. *Prog Phys Geogr* 26:47–75

- 860 Walker IJ, Hesp PA, Davidson-Arnott RG, Ollerhead J (2006) Topographic  
861 steering of alongshore airflow over a vegetated foredune: Greenwich dunes,  
862 prince edward island, canada. *Journal of Coastal Research* 22:1278–1291
- 863 Walker IJ, Hesp PA, Davidson-Arnott RG, Bauer BO, Namikas SL, Ollerhead  
864 J (2009) Responses of three-dimensional flow to variations in the angle of  
865 incident wind and profile form of dunes: Greenwich dunes, prince edward  
866 island, canada. *Geomorphology* 105:127–138
- 867 Walmsley JL, Salmon J, Taylor P (1982) On the application of a model of  
868 boundary-layer flow over low hills to real terrain. *Boundary-Layer Meteorol*  
869 23:17–46
- 870 Weaver C, Wiggs G (2011) Field measurements of mean and turbulent airflow  
871 over a barchan sand dune. *Geomorphology* 128:32–41
- 872 Werner BT, Kocurek G (1999) Bedform spacing from defect dynamics. *Geol-*  
873 *ogy* 27:727–730
- 874 Wiggs G, Bullard J, Garvey B, Castro I (2002) Interactions between airflow  
875 and valley topography with implications for aeolian sediment transport.  
876 *Physical Geography* 23:366–380
- 877 Wood N (2000) Wind flow over complex terrain: a historical perspective and  
878 the prospect for large-eddy modelling. *Boundary-Layer Meteorol* 96:11–32
- 879 Zhang C, Li Q, Zhou N, Zhang J, Kang L, Shen Y, Jia W (2016) Field obser-  
880 vations of wind profiles and sand fluxes above the windward slope of a sand  
881 dune before and after the establishment of semi-buried straw checkerboard  
882 barriers. *Aeolian Res* 20:59–70
- 883 Zilker DP, Hanratty TJ (1979) Influence of the amplitude of a solid wavy wall  
884 on a turbulent flow. part 2. separated flows. *J Fluid Mech* 90:257–271
- 885 Zilker DP, Cook GW, Hanratty TJ (1977) Influence of the amplitude of a solid  
886 wavy wall on a turbulent flow. part 1. non-separated flows. *J Fluid Mech*  
887 82:29–51

---

888      **Local wind regime induced by giant linear dunes**  
 889      — Supplementary Material —

890    **C. Gadal\*** · P. Delorme · C. Narteau · G.F.S. Wiggs · M. Baddock ·  
 891    J.M. Nield · P. Claudin

892

893    \* Institut de Mécanique des Fluides de Toulouse, Université de Toulouse Paul  
 894    Sabatier, CNRS, Toulouse INP-ENSEEIHT, Toulouse, France.

895    [cyril.gadal@imft.fr](mailto:cyril.gadal@imft.fr)

896    **1. Shear velocity and calibration of the hydrodynamical roughness**

897    As the regionally predicted and locally measured velocities are available at  
 898    different heights, we can not compare them directly. We therefore convert  
 899    all velocities into shear velocities  $u_*$ , characteristic the turbulent logarithmic  
 900    velocity profile (Spalding 1961; Stull 1988):

$$\frac{u(z)}{u_*} = \frac{1}{\kappa} \ln \left( \frac{z}{z_0} \right), \quad (15)$$

901    where  $z$  is the vertical coordinate,  $\kappa = 0.4$  the von Kármán constant and  $z_0$  the  
 902    hydrodynamic roughness. Note that, strickly speaking, this logarithmic profile  
 903    is valid for a neutrally stratified ABL only. Vertical density gradients occurring  
 904    in other conditions may thus induce large discrepancies (Monin and Obukhov  
 905    1954; Garratt 1994; Dyer 1974). However, as our wind measurements are in  
 906    the flow region close enough to the surface, where these effects are negligible,  
 907    this logarithmic wind profile remains a fairly good approximation in all conditions  
 908    (Gunn et al. 2021b). Several measurements of hydrodynamic roughnesses  
 909    are available (Raupach 1992; Bauer et al. 1992; Brown et al. 2008; Nield et al.  
 910    2014). In the absence of sediment transport, it is governed by the geometric  
 911    features of the bed (Flack and Schultz 2010; Pelletier and Field 2016). When  
 912    aeolian saltation occurs, it is rather controlled by the altitude of Bagnold's  
 913    focal point (Durán et al. 2011; Valance et al. 2015), which depends on the  
 914    wind velocity and grain properties (Sherman and Farrell 2008; Zhang et al.  
 915    2016; Field and Pelletier 2018). Whether associated with geometric features  
 916    or with sediment transport, its typical order of magnitude is the millimetre  
 917    scale on sandy surfaces.

918    We do not have precise velocity vertical profiles to be able to deduce an  
 919    accurate value of  $z_0$  in the various environments of the meteorological stations  
 920    (vegetated, arid, sandy). Our approach is to rather select the hydrodynamic  
 921    roughness which allows for the best possible matching between the regionally  
 922    predicted and locally measured winds, i.e. minimising the relative difference  $\delta$   
 923    between the wind vectors of both datasets:

$$\delta = \frac{\sqrt{\langle \| \mathbf{u}_{*,\text{era}} - \mathbf{u}_{*,\text{station}} \|^2 \rangle}}{\sqrt{\langle \| \mathbf{u}_{*,\text{era}} \|^2 \rangle \langle \| \mathbf{u}_{*,\text{station}} \|^2 \rangle}}, \quad (16)$$

where  $\langle \cdot \rangle$  denotes time average. This parameter is computed for values of  $z_0$  in ERA5-Land analysis ranging from  $10^{-5}$  m to  $10^{-2}$  m for the four different stations. Note that for the North Sand Sea and South Sand Sea stations, where the giant dunes feedback presumably affect the wind, we take into account the non-deflected winds only in the calculation of  $\delta$  (with a  $15^\circ$  tolerance).

As shown in Online Resource Fig. S3, the minimum values of  $\delta$  in the space  $(z_0^{\text{ERA5Land}}, z_0^{\text{local}})$  form a line. We thus set the roughness in the ERA5-Land analysis to the typical value  $z_0 = 10^{-3}$  m, and deduce the corresponding ones for the local stations. It leads to 2.7, 0.8, 0.1 and 0.5 mm for the Etosha West, North Sand Sea, Huab and South Sand Sea stations, respectively. Importantly, this approach somewhat impacts the calculation of the shear velocities, but not that of the wind directions. As such, most of our conclusions are independent of such a choice. However, it may affect the magnitude of the wind velocity attenuation/amplification in flow confinement situations.

## 2. Computation of the ABL characteristics

The estimation of the non-dimensional numbers associated with the ABL requires the computation of representative meteorological quantities. In arid areas, the vertical structure of the atmosphere can be approximated by a well mixed convective boundary layer of height  $H$ , topped by the stratified free atmosphere (Stull 1988; Shao 2008). In this context, one usually introduces the virtual potential temperature  $T_{\text{vp}}$ , which is a constant  $T_0$  inside the boundary layer, and increases linearly in the FA (Online Resource Fig. S8a):

$$T_{\text{vp}}(z) = \begin{cases} T_0 & \text{for } z \leq H, \\ T_0 \left(1 + \frac{\Delta T_{\text{vp}}}{T_0} + \frac{N^2}{g}(z - H)\right) & \text{for } z \geq H, \end{cases} \quad (17)$$

where  $\Delta T_{\text{vp}}$  is the temperature discontinuity at the capping layer and  $N = \sqrt{g\partial_z T_{\text{vp}}/T_0}$  is the Brunt-Väisälä frequency, characteristic of the stratification. Note that, under the usual Boussinesq approximation, temperature and air density variations are simply related by  $\delta T_{\text{vp}}/T_0 \simeq -\delta\rho/\rho_0$  (see Online Resource of Andreotti et al. (2009)), so that  $N$  can equivalently be defined from the density gradient as next to (1).

The ERA5 dataset provides vertical profiles of the geopotential  $\phi$ , the actual temperature  $T$  and the specific humidity  $\eta$  at given pressure levels  $P$ . The vertical coordinate is then calculated as:

$$z = \frac{\phi R_t}{g R_t - \phi}, \quad (18)$$

where  $R_t = 6371229$  m is the reference Earth radius and  $g = 9.81$  m s $^{-2}$  is the gravitational acceleration. One also computes the virtual potential temperature as:

$$T_{\text{vp}} = T \left[1 + \left(\frac{M_d}{M_w} - 1\right) \eta\right] \left(\frac{P_0}{P}\right)^{R/C_p}, \quad (19)$$

where  $P_0 = 10^5$  Pa is the standard pressure,  $R = 8.31$  J/K is the ideal gas constant,  $C_p \simeq 29.1$  J/K is the air molar heat capacity, and  $M_w = 0.018$  kg/Mol and  $M_d = 0.029$  kg/Mol are the molecular masses of water and dry air respectively. The specific humidity is related to the vapour pressure  $p_w$  as

$$\eta = \frac{\frac{M_w}{M_d} p_w}{p - \left(1 - \frac{M_w}{M_d}\right) p_w}. \quad (20)$$

The ERA5 dataset also provides an estimate of the ABL depth  $H$ , based on the behaviour of the Richardson vertical profile. This dimensionless number is defined as the ratio of buoyancy and flow shear terms, and can be expressed as  $\text{Ri} = N^2 / (\partial_z u)^2$ . It vanishes in the lower well-mixed layer where  $T_{\text{vp}}$  is constant, and increases in the stratified FA. Following the method and calibration of Vogelegang and Holtlag (1996); Seidel et al. (2012), the value  $\text{Ri}(z) \simeq 0.25$  has been shown to be a good empirical criterion to give  $z \simeq H$  within a precision varying from 50% for the shallower ABL (e.g. at night) to 20% for situations of stronger convection.

Examples of vertical profiles of the virtual potential temperature deduced from ERA5 are shown in Online Resource Fig. S8a. For each of them, an average temperature is computed below the ABL depth ( $z < H$ ), and a linear function is fitted above, allowing us to extract the temperature jump  $\Delta T_{\text{vp}}$ . Importantly, some profiles display a vertical structure that cannot be approximated by the simple form (17) used here (Online Resource Fig. S8b). In practice, we removed from the analysis all of those leading to the unphysical case  $\Delta T_{\text{vp}} < 0$ . We have noticed that these ‘ill-processed’ profiles dominantly occur in winter and are evenly spread across the hours of the day. Importantly, they represent  $\simeq 12\%$  of the data only (Online Resource Fig. S8c,d), and we are thus confident that this data treatment does not affect our conclusions.

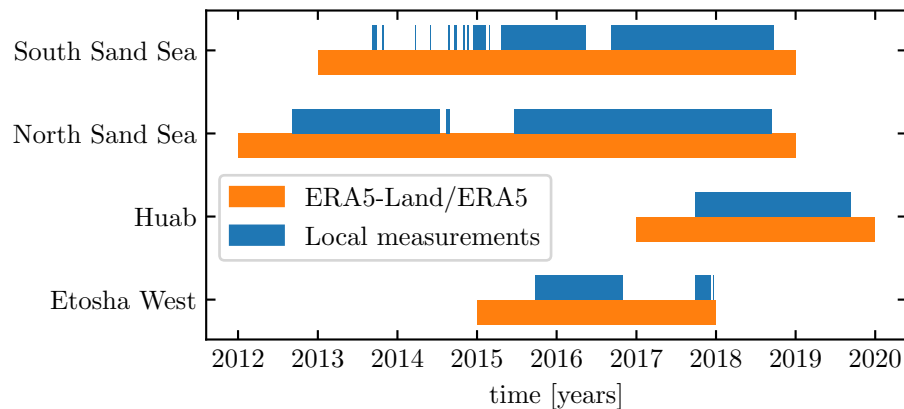


**Fig. S1** Gant chart representing the valid time steps for the two data sets, for all stations.

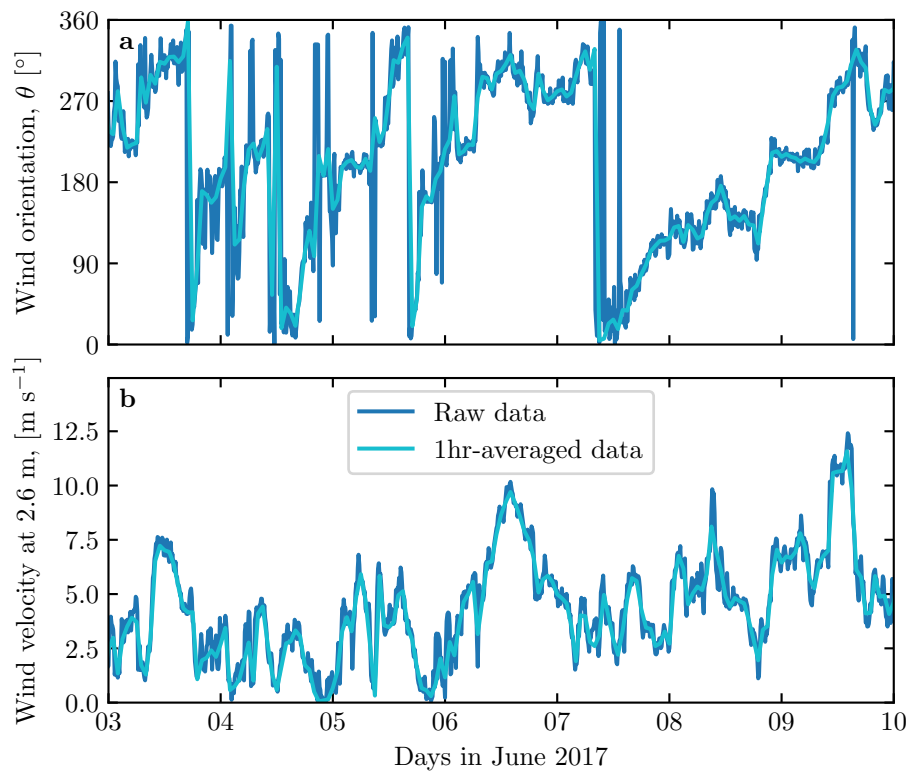


**Fig. S2** Local wind measurements: comparison between raw (blue) and hourly-averaged (light blue) data from South Sand Sea station. **a:** wind direction. **b:** wind velocity at height 2.6 m.

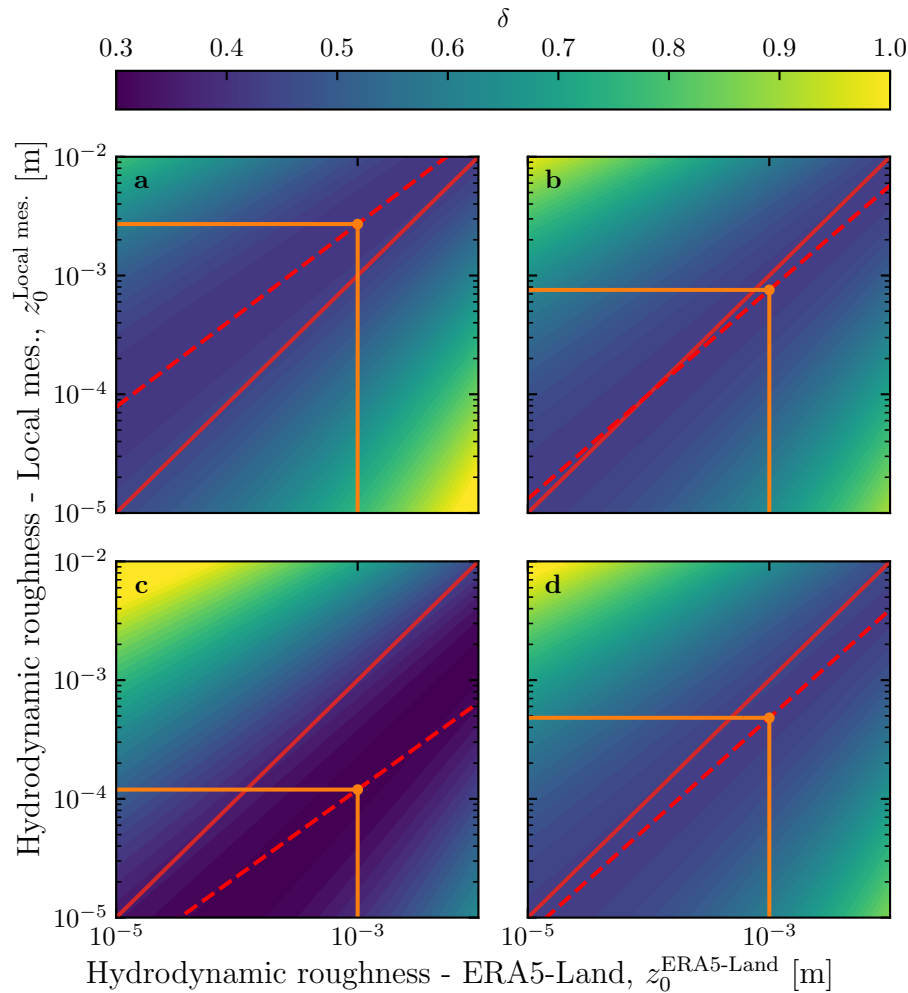


**Fig. S3** Calibration of hydrodynamic roughness. The parameter  $\delta$  (16) quantifying the difference between local and predicted winds is shown in color scale as a function of the hydrodynamic roughnesses chosen for the ERA5-Land and for local winds, for the (a) Etosha West, (b) North Sand Sea, (c) Huab and (d) South Sand Sea stations. The red dashed and plain lines shows the minima of  $\delta$  and the identity line, respectively. The orange lines and dots highlight the chosen hydrodynamic roughnesses for the local winds deduced from setting  $z_0^{\text{ERA5-Land}} = 1 \text{ mm}$ .

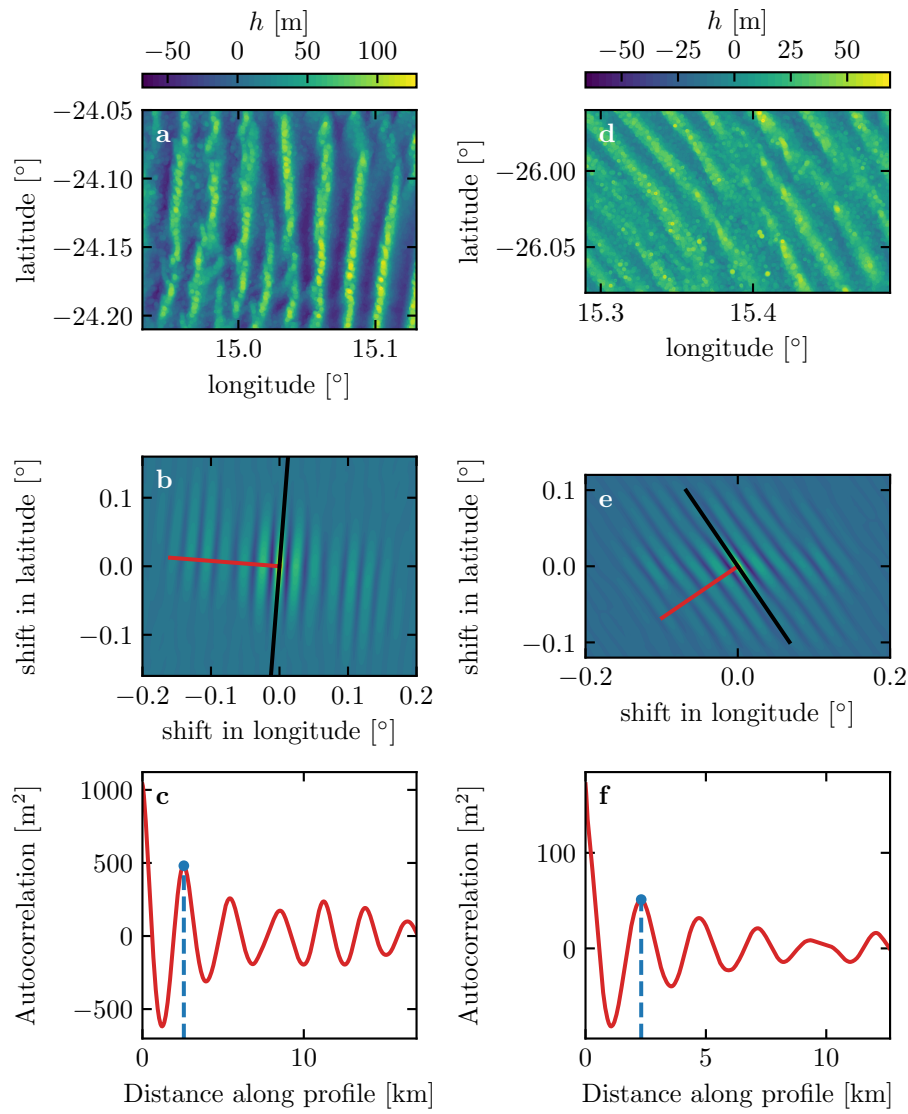


**Fig. S4** Analysis of the DEMs of the North Sand Sea (left column – panels **a**, **b**, **c**) and South Sand Sea (right column – panels **d**, **e**, **f**) stations. **a–d**: Bed elevation detrended by a fitted second order polynomial base-line. **b–e**: Autocorrelation matrix shown in color scale. The black line shows the detected dune orientation, and the red line represents the autocorrelation profile along which the dune wavelength is calculated, displayed in **c–f**. The blue lines and dots show the first peak of the autocorrelation profile, whose abscissa gives the characteristic wavelength of the dune pattern.

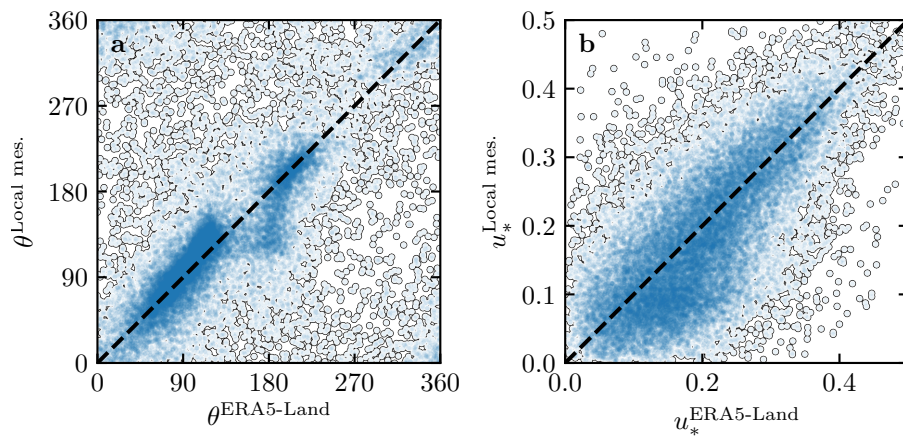


**Fig. S5** Statistical comparison of the wind orientation (a) and velocity (b) between the ERA5-Land dataset and the local measurements for the Huab and Etosha West stations. Data point clustering around identity lines (dashed and black) provide evidence for agreement of the two sets.

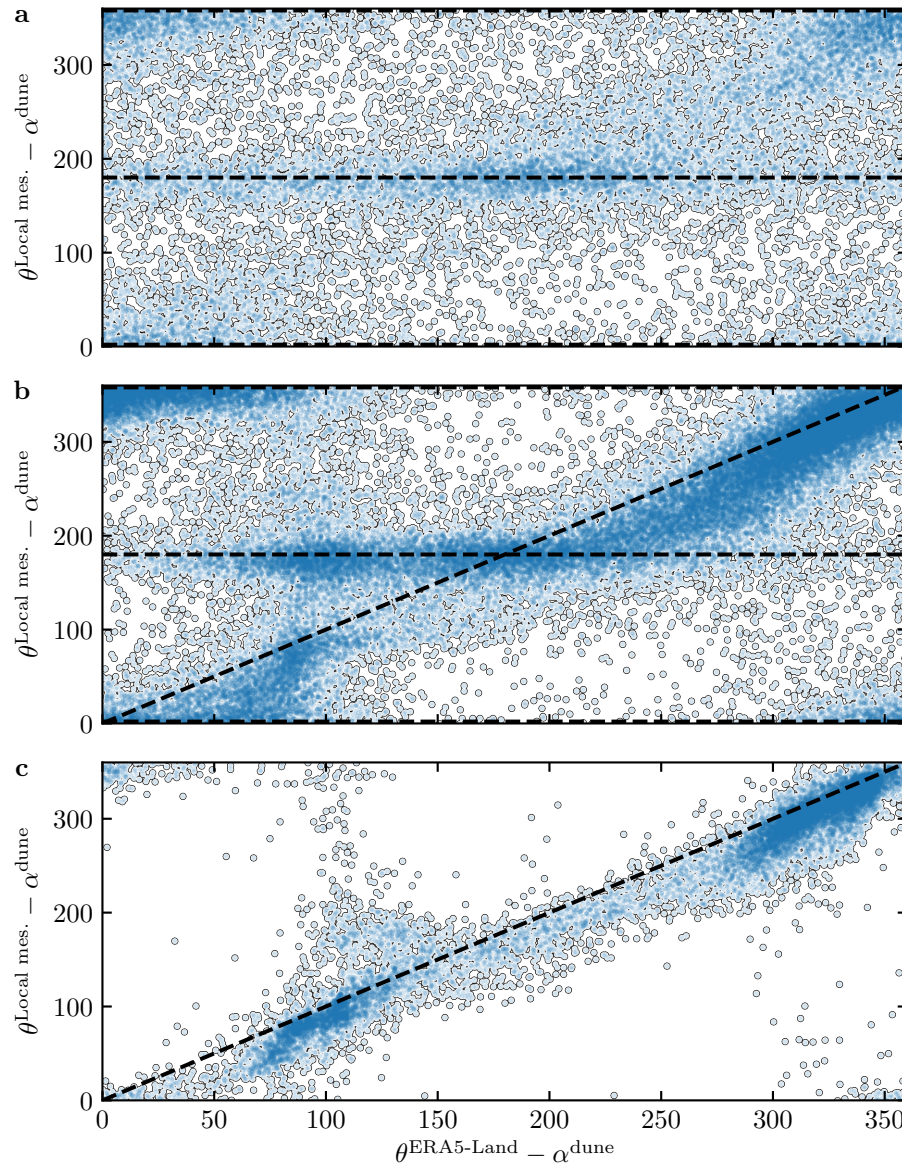


**Fig. S6** Statistical comparison of the wind orientation between the ERA5-Land dataset and the local measurements for the South Sand Sea and North Sand Sea stations, for different velocity ranges. **a:**  $u^{\text{ERA5-Land}}_* < 0.1 \text{ m s}^{-1}$ . **b:**  $0.1 < u^{\text{ERA5-Land}}_* \leq 0.25 \text{ m s}^{-1}$ . **c:**  $u^{\text{ERA5-Land}}_* \geq 0.25 \text{ m s}^{-1}$ . The measured dune orientations are subtracted to the wind orientation, which allows us to plot both stations on the same graph. Black dashed lines indicate locally measured orientations aligned with the dune crests (here  $0^\circ$ ,  $180^\circ$  and  $360^\circ$  – panels **a**, **b**), as well as the identity lines (panels **b**, **c**).

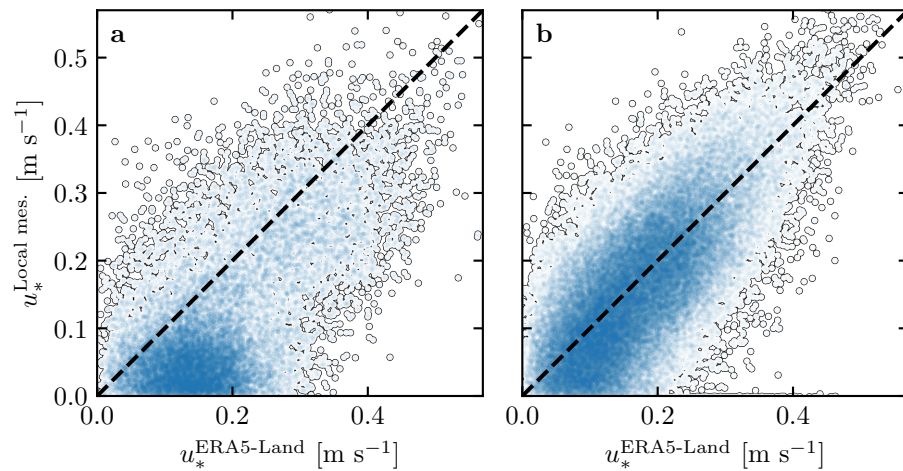


**Fig. S7** Statistical comparison of the wind velocity between the ERA5-Land dataset and the local measurements for the South Sand Sea and North Sand Sea stations. **a:** Nocturnal summer easterly wind. **b:** Diurnal southerly wind. Black dashed lines are identity lines. The angle ranges used to select diurnal and nocturnal summer winds are the same as those in Figs. 4 and Figs. 6 of the main article.

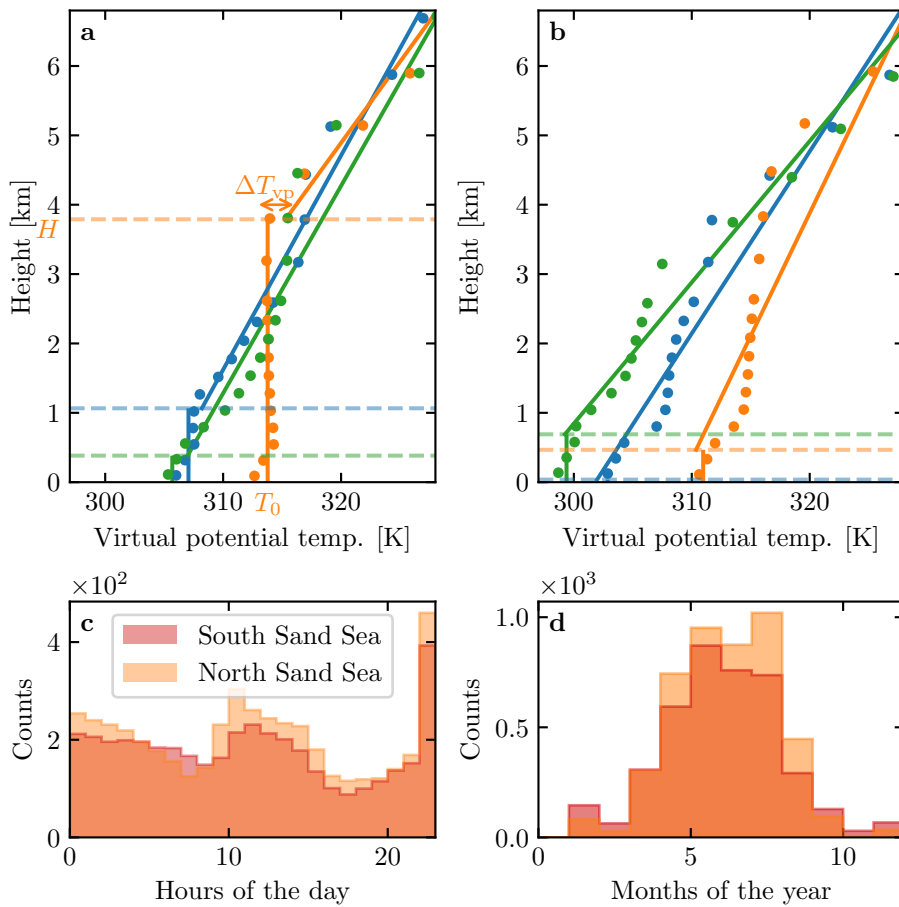


**Fig. S8** **a:** Vertical profiles of the virtual potential temperature at three different times (blue: 29/11/2012 - 11.00 UTC, orange: 21/03/2017 - 12.00 UTC, green: 21/03/2017 - 20.00 UTC) at the South Sand Sea station. Dots: data from the ERA5 reanalysis. Dashed lines: boundary layer height given by the ERA5 reanalysis. Plain lines: vertical (ABL) and linear (FA) fits to estimate the quantities displayed in Online Resource Fig. S9. **b:** Examples of ill-processed vertical profiles at three different times (blue: 2/12/2013 - 23.00 UTC, orange: 20/03/2017 - 00.00 UTC, green: 14/07/2017 - 14.00 UTC) at the South Sand Sea station. Distribution of ill-processed vertical profiles at South (orange) and North (light orange) Sand Sea station: hourly **(c)** and monthly **(d)** counts.

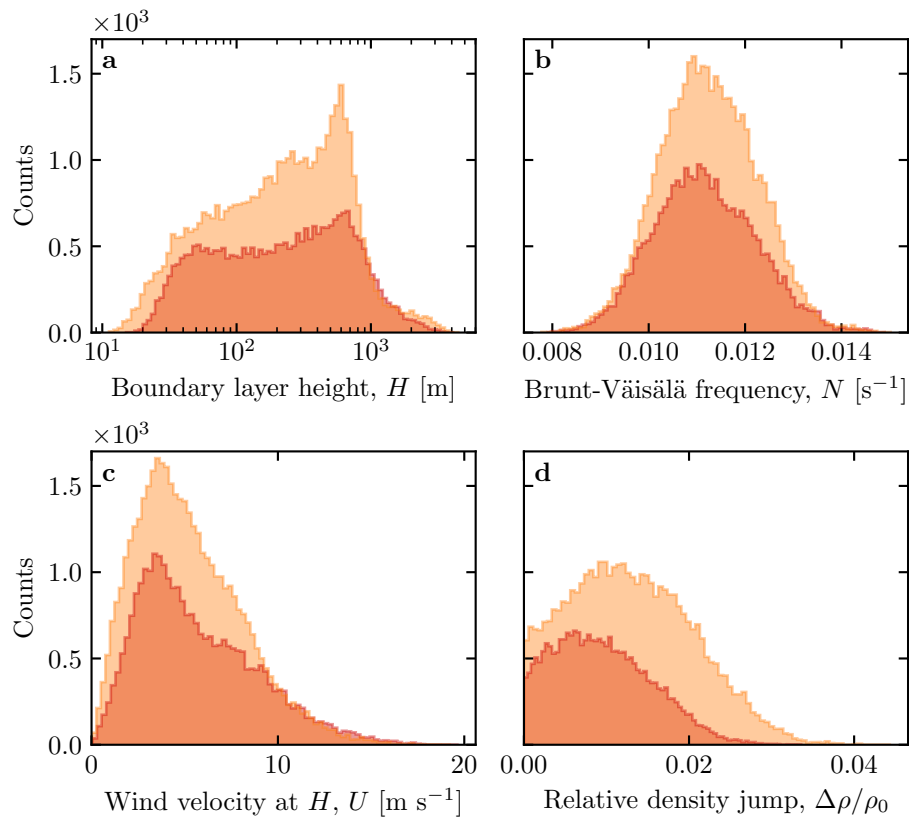


**Fig. S9** Distributions of the meteorological parameters resulting from the processing of the ERA5-Land data for the South Sand Sea (orange) and the North Sand Sea (light orange) stations.

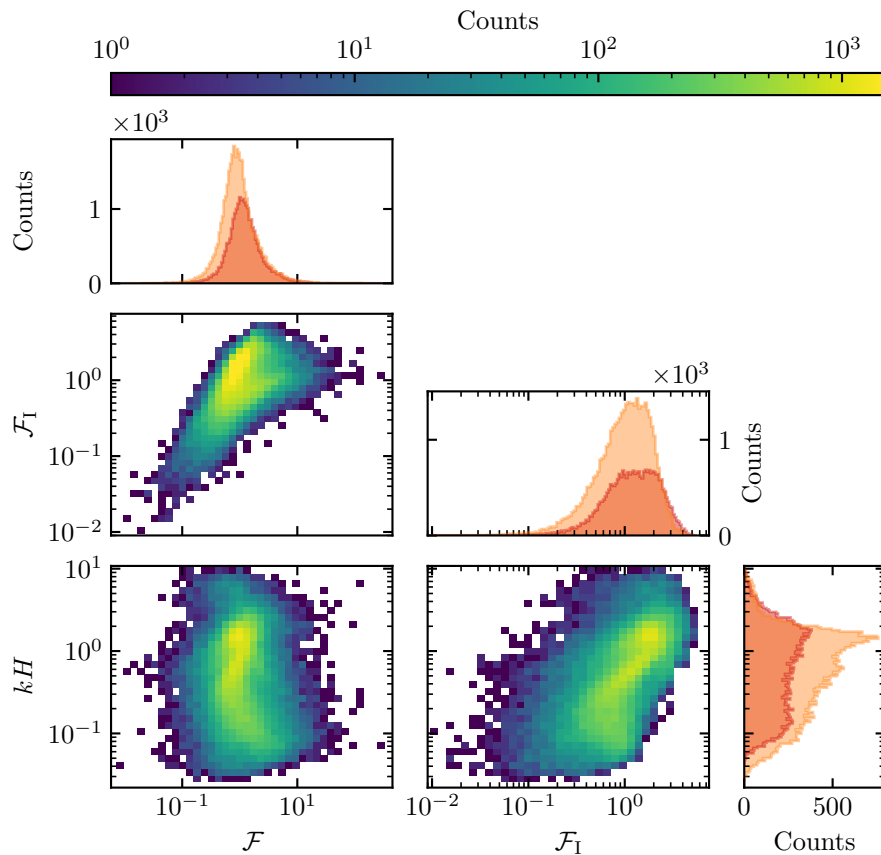


**Fig. S10** Non-dimensional parameters distributions. For the marginal distributions, the light orange corresponds to the South Sand Sea station, and the orange to the North Sand Sea station.

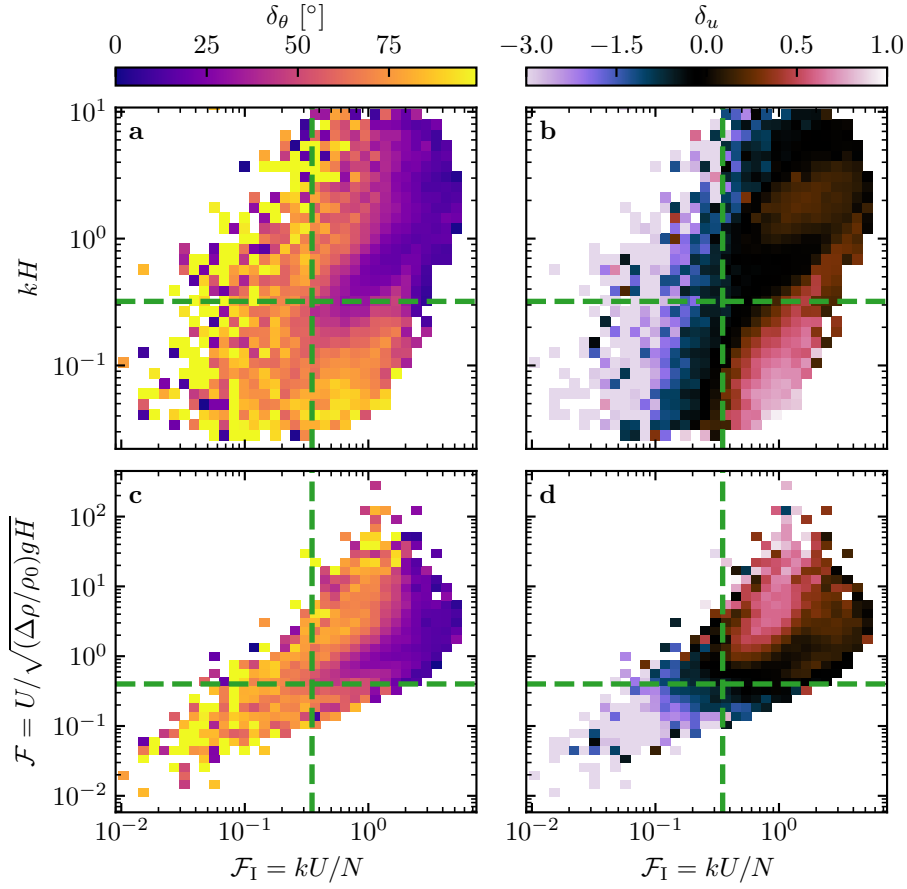


**Fig. S11** Regime diagrams of the wind deviation  $\delta_\theta$  and relative attenuation/amplification  $\delta_u$  in the spaces  $(\mathcal{F}_I, kH)$  and  $(\mathcal{F}_I, \mathcal{F})$ , containing the data from both the North Sand Sea and South Sand Sea stations. Green dashed lines empirically delimit the different regimes. The point density in each bin of the diagrams is shown in Online Resource Fig. S10 – 95% of the data occur in the range  $-1 < \delta u < 1$ . The similar regime diagrams in the space  $(\mathcal{F}, kH)$  are shown in Fig. 8.

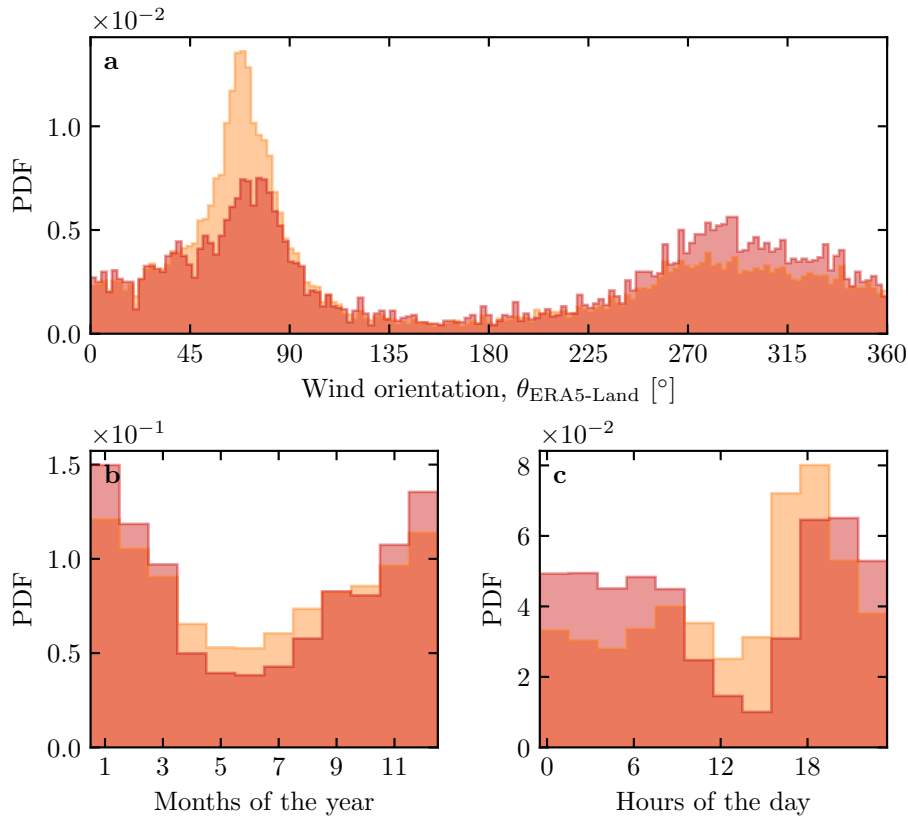


**Fig. S12** Normalized distributions of amplified velocities for the North sand Sea (light orange:  $\delta_u < 0$ , orange:  $\delta_u < -0.5$ ). **a:** Angular distributions. **b:** Monthly distributions. **c:** Hourly distributions.

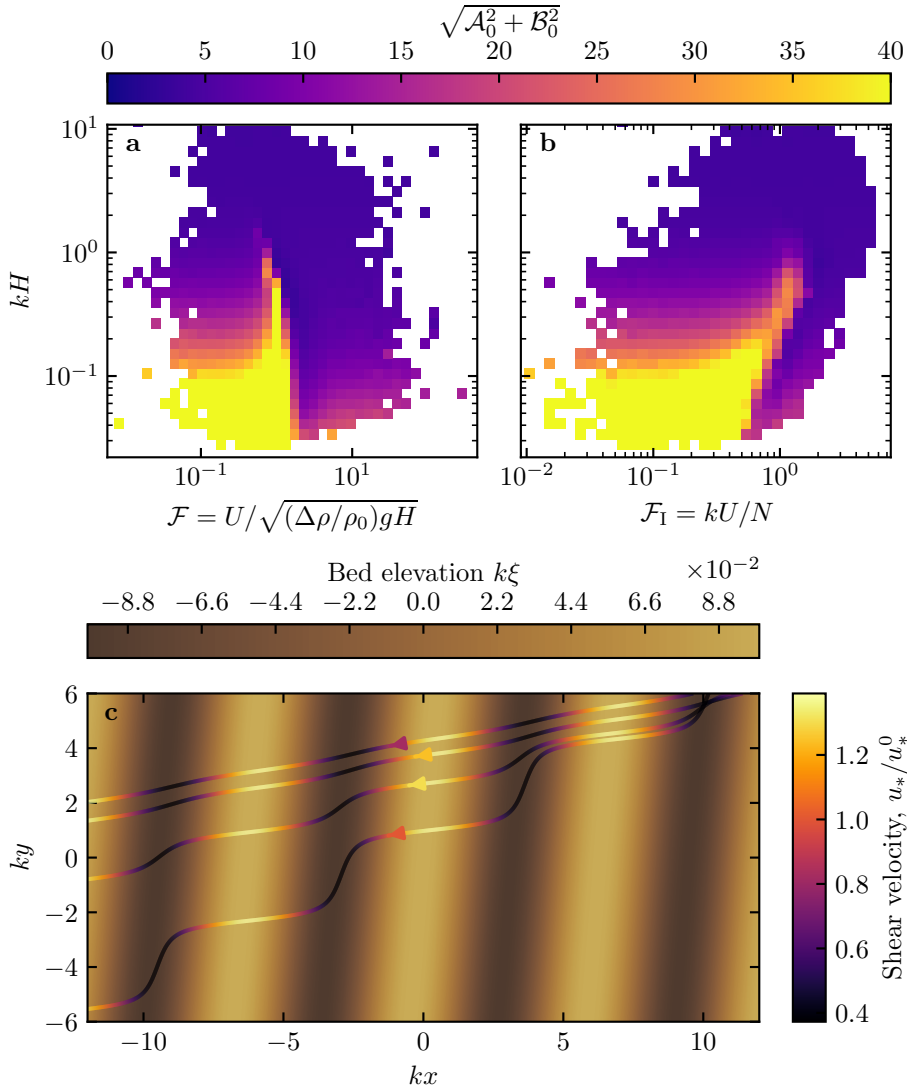


**Fig. S13** Computation of the flow disturbance with the linear model of Andreotti et al. (2009). **a–b:** Magnitude of the hydrodynamic coefficients  $A_0$  and  $B_0$ , calculated from the time series of the non-dimensional numbers corresponding to the ERA5-Land wind data and ERA5 data on vertical pressure levels. **c** Shear velocity streamlines over sinusoidal ridges of amplitude  $k\xi_0 = 0.1$  and for increasing values of  $\sqrt{A_0^2 + B_0^2}$ . From the upper to the lower streamline, values of  $(kH, \mathcal{F}, \mathcal{F}_I, A_0, B_0, \sqrt{A_0^2 + B_0^2})$  are  $(1.9, 0.6, 1.5, 3.4, 1.0, 3.5)$ ,  $(1.5, 0.3, 0.4, 4.8, 1.4, 5.0)$ ,  $(0.1, 3.5, 1.0, 8.6, 0.1, 8.6)$ ,  $(0.5, 0.05, 0.04, 9.6, 2.5, 9.9)$ .

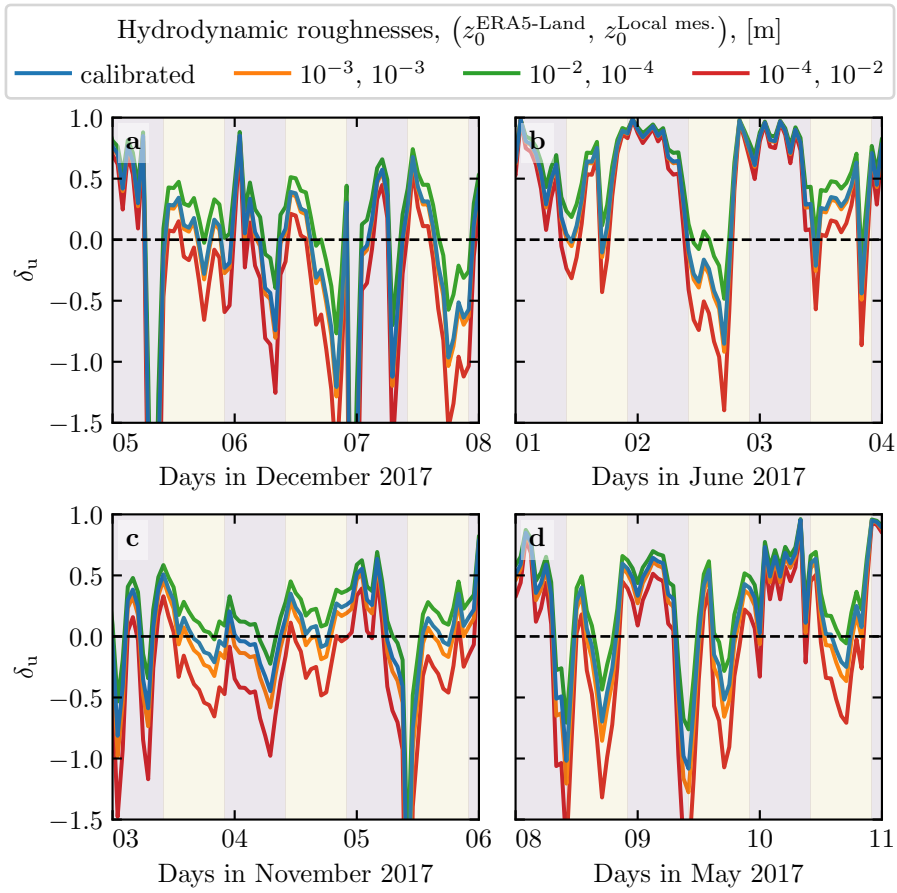


**Fig. S14** Time series of the relative velocity disturbance  $\delta_u$  corresponding to Fig. 5, for different values of the hydrodynamic roughnesses. **a:** North Sand Sea – summer, **b:** North Sand Sea – winter, **d:** South Sand Sea – summer, **e:** South Sand Sea – winter. Note that  $\delta_\theta$  is independent of the choice of  $z_0^{\text{ERA5-Land}}$  and  $z_0^{\text{Local mes.}}$ .